Heliyon 10 (2024) e24607

Contents lists available at ScienceDirect

Heliyon

journal homepage: www.cell.com/heliyon

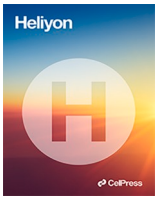

Research article

Comparative investigations of electronic, mechanical and optical responses of Ra-doping in Barium Titanate for optoelectronic applications: A computational insight

Muhammad Moin [a,*], Abdul Waheed Anwar [b], Mehrunisa Babar [b], Udayabhaskararao Thumu [a], Anwar Ali [b]

[a] Institute of Fundamental and Frontier Sciences, University of Electronic Science and Technology of China, Chengdu, 610054, China
[b] Department of Physics, University of Engineering and Technology, Lahore, Pakistan

ARTICLE INFO

Keywords:
BTO
Refractive index
Kleinman coefficient
Optical coefficients
Born stability

ABSTRACT

This unique study examined the theoretical pure $BaTiO_3$ and doped Ra ($Ba_{1-x}Ra_xTiO_3$) impact on electronic, mechanical and optical responses were using Heydscuseria-Ernzerhof screened hybrid functional (HSE06) and generalized gradient approximation (GGA-PBE) with norm-converging pseudopotential approaches in the density functional theory. Computed the lattice constant and bond lengths for pure ($BaTiO_3$) and doped atoms as well as explored the changes of consequences of electronic, mechanical and optical responses. The calculated values indicate the $BaTiO_3$ is an indirect characteristic and an optically inactive nature. The low energy state and also conduction band of the crystal structure to transform to the direction of low energy and narrows the electronic band gap. The bandgap of pure $BaTiO_3$ is continually reduced which shifts the Fermi energy level E_g. When increasing the doping impurities (x) of (Ra) in $BaTiO_3$, the band gap shifts from indirect (X-G) to direct (X-X) nature and become optically active. The elastic and mechanical responses are essential for suitable (Ra) doped material ensuring structural integrity and predicting a ductile behavior. Kleinman coefficient (ξ), it is clear that (Ra)-doped materials shows slightly large resistance to bond bending and bond angle distortion as compare to pure $BaTiO_3$. Optical characteristics of the both pure and doped (Ra) materials in the core level spectra are thoroughly investigated. Optical coefficients are obtained in the energy scale start from 0 to 20 eV. Moreover, the results of optical properties show excellent influence of doping so that this material can be employed as UV filter in the UV region and in optoelectronics devices.

1. Introduction

$BaTiO_3$, also known as barium titanate, is a ferroelectric ceramic material that has been extensively researched and studied by scientists and researchers [1]. It has a perovskite crystal structure, consisting of one barium (Ba) atom, one titanium (Ti) atom, and three oxygen (O) atoms. The ferroelectric properties of $BaTiO_3$ are a result of its spontaneous polarization, which can be switched by applying an external electric field [2]. This makes it a valuable material for various technological applications, including electronic devices, energy storage, sensors, actuators, and memory devices [3]. Researchers have been interested in $BaTiO_3$ due to its unique

* Corresponding author.
E-mail address: moingcs786@gmail.com (M. Moin).

https://doi.org/10.1016/j.heliyon.2024.e24607
Received 16 August 2023; Received in revised form 10 January 2024; Accepted 10 January 2024
Available online 18 January 2024

properties and potential applications. Here are some key areas of research related to $BaTiO_3$ Ferroelectricity and Phase Transitions $BaTiO_3$ exhibits multiple phase transitions as the temperature changes. Researchers have investigated the structural and electrical properties of these different phases, such as the tetragonal, cubic, and rhombohedral phases, to understand the underlying mechanisms and the relationship between structure and functionality. $BaTiO_3$ thin films and nanostructures have attracted significant attention for their potential use in microelectronic devices [4]. Researchers have explored various deposition techniques to fabricate high-quality films with controlled properties, such as epitaxial growth, sol-gel processing, pulsed laser deposition, and chemical vapor deposition [5]. Multiferroicity Materials like $BaTiO_3$ is not inherently a magnetic material, but researchers have explored ways to induce magnetism in BaTiO3-based composites by introducing magnetic elements. These multiferroicity materials can exhibit both ferroelectric and magnetic properties, enabling new functionalities and applications, such as magneto electric coupling. $BaTiO_3$ has been investigated as a potential material for energy storage applications, such as capacitors and dielectric materials [6]. Researchers have explored ways to increase the dielectric constant, breakdown strength, and energy storage density of $BaTiO_3$-based materials to improve their performance in energy storage devices. The piezoelectric response of $BaTiO_3$ and developed applications such as piezoelectric sensors, actuators, and energy harvesters. Overall, the research on $BaTiO_3$ has focused on understanding its fundamental properties, improving its performance, and exploring novel applications. This versatile material continues to be an important subject of study for researchers in various scientific and engineering fields. The general formula of perovskite materials ABX_3 crystal structures represent large flexibility and also large capacity to host ions of different sizes and large scale of dopants (Ra) can be incorporated at the Ba site in $BaTiO_3$ respectively. Trivalent rare-earth dopants in particular have drawn a lot of interest due to their versatility as donors and acceptors [7]. It has been suggested that adding a modest amount of rare-earth dopants to $BaTiO_3$ systems can significantly enhance the dielectric characteristics, mechanical properties, sintering properties, phase composition, and microstructure of ceramic materials. Given their evident significance, several experimental and theoretical investing at ions based on BTO materials have been accomplished with adjusting the physical and chemical and electrical responses using various dopants. Islam, Suravi et al. have created ($Ba_{1-x}Y_xTiO_3$) solubility associated with the electron compensation utilizing 007 A a solid-state reaction technique [8]. They claimed that doping Y at site A can produce high conductivity, which is followed by a huge permittivity and a significant amount of dielectric loss [9]. As a result, it was discovered that each rare-earth element had a crucial impact on the dielectric characteristics, with $Ba_{0.75}Ra_{0.25}TiO_3$, $Ba_{0.50}Ra_{0.50}TiO_3$ and $Ba_{0.25}Ra_{0.75}TiO_3$ doping exhibiting the greatest leakage current in comparison to other rare-earth elements. There have been numerous researchers who have studied the electronic, mechanical, and optical properties of pure and doped Barium Titanate ($BaTiO_3$) for various optoelectronic applications [10,11]. They have explored various doping techniques and investigated the influence of dopants on the electrical conductivity, optical bandgap, and piezoelectric properties of BTO. They have focused on enhancing the material's optoelectronic performance and developing novel applications based on these properties. Ram S. Katiyar et al. have carried out extensive research on the electronic, optical, and photovoltaic responses of pure and doped BTO films [12]. They have studied the influence of doping elements on the structural, electrical, and optical characteristics of these materials for potential optoelectronic applications. Hao Zhang et al. has conducted research on BTO-based ceramics and thin films for optoelectronic applications [13]. They have explored the influence of dopants on the material's optical properties, such as refractive index, transparency, and luminescence, and studied their potential for optical waveguides and sensors. The main objective of my research work to explore the doping effect on BTO for electronic, mechanical, and optical properties in optoelectronic applications.

1.1. Computational background

The first principles are based on the Hybrid functional (HSE06) and Generalized Gradient Approximation (GGA-PBE), which Perdew–Burke Erznerhoff et al. disclosed Using the Plane-Wave Pseudo-Potential Method [14]. The Norm-conserving and ultrasoft pseudo-potentials (USP) gives a frozen core approximation hierarchy and the estimation of electron-ion interactions needed only comparably a restricted number of the Fourier components [15]. The pure ($BaTiO_3$) and $Ba_{0.75}Ra_{0.25}TiO_3$, $Ba_{0.50}Ra_{0.50}TiO_3$ and $Ba_{0.25}Ra_{0.75}TiO_3$-doped atoms have face-centered cubic crystal structures of space group Fm3m (225) [28]. With the crystal structure of Barium Titanate (BaTiO3), was in the (Ba) atoms are at the corner of the cubic and are coordinated by its eight equivalent nearest neighbor oxygen (O) atoms and the Oxygen (O) atoms are tetrahedral coordinated by four (Ba, Ti) atoms [16]. With norm converging pseudopotential was employed with the hybridization configurations of [Ba]: $5s^2$, $5\ p^6$, $6s^2$, [Ti]: $3s^2$, $3p^6$, $3\ d^2$, $4s^2$ and [O]: $2s^2$, $2p^4$. Barium Titanate (BaTiO3) and doped for both materials, and a plane wave basis set with cut-off energy 480eV (GGA) and 840eV (HSE06) are applied [17,18]. The Brillouin zone was sampled by ($6 \times 6 \times 1$) mesh of k-points [19]. It is worth noting that the computational methodology outlined above provides a general framework, and the specific details may vary depending on the software package and parameters used for the calculations. It is always important to validate the results and compare them with experimental data. During the geometry optimization, the energy change is smaller than (5×10^{-6}) eV $atom^{-1}$, extreme force over each atom below (0.01eV) $Å^{-1}$ pressure less than (0.02 GPa) and extreme atomic displacement not increasing (5×10^{-4}) Å. $BaTiO_3$ has a cubic and this The geometry of ($2 \times 2 \times 1$) supercell with residual force of SCF (1×10^{-6}) eV was adjusted at different parameters by energy convergence. In literature [21,26] further computational set-up is conceivable [20].

1.2. Structural properties

The first step involves optimizing the crystal structure of cubic $BaTiO_3$ using DFT calculations. This involves determining the most stable arrangement of atoms by minimizing the total energy of the system. The lattice parameters, which describe the size and shape of the unit cell, are adjusted during this optimization process [21]. The geometry optimization cubic system of $BaTiO_3$ has been shown in Fig. 1.

Fig (a, b) the geometry optimized simple and 2 × 2 × 1 crystal structure of $BaTiO_3$ using GGA and HSE06 functional. The valence of Radium used here (Ra^{+2}) atoms were replaced for (Ba^{+2}) sites. Subsequently, calculate of the stability of BTO crystal structure main concept is the tolerance factor which computed by using following expression [22].

$$t = \frac{r_{0+r_A}}{\sqrt{2}\,(r_{0+r_A})} \tag{1}$$

here, r_A and r_B are called the ionic radius of (A: Ba) and (B: Ti) sites, whereas r_0 is denote the ionic radii of oxygen atom [23]. Under stable ABX_3 crystal system the tolerance factor is obtained in the limit of $0.87 < t < 1.12$, and the cubic (BTO) system value range to $t = 1.0$ respectively [24]. The tolerance factor (t) deviates from this limit, the (BTO) system will be distorted due to the incline of the (BO_6) octahedron, convincing a crystal s change to a non-perovskite system [25]. Ba atoms are situated at the cube corner, Ti atoms are in the centre of the cube, and O atoms are in the centres of the faces. The computed lattice parameter values and total energy of pure and doped- $Ba_{0.75}Ra_{0.25}TiO_3$, $Ba_{0.50}Ra_{0.50}TiO_3$ and $Ba_{0.25}Ra_{0.75}TiO_3$ at T = 0 k are shown in Fig. 2.

As the number of optimization steps increases, the energy of the unit cell increases and the system starts to approach volatility, as shown in Fig. 2. As the volume keeps increasing and the system gets closer to volatility, the energy of the unit cell increases. The reported experimental and theoretical data are also discussed in Table 1 for comparison.

The computed lattice constants are in comparable with the calculated experimental value of the lattice parameters a = b = 4.00 Å, c = 4.024 Å, a = b = 4.007 Å and c = 4.186 Å. Currently, calculated the lattice constant values and cell volume are justified in the above table the lattice coefficients, which are a = b = 4.067 Å and c = 4.308 Å and bond length 2.366 Å. After doping impurities of $Ba_{0.75}Ra_{0.25}TiO_3$, $Ba_{0.50}Ra_{0.50}TiO_3$ and $Ba_{0.25}Ra_{0.75}TiO_3$-doped atoms we justified that the calculated of cell volume values is 67.44 $Å^3$, 66.85 $Å^3$, 65.82 $Å^3$ and 65.85 $Å^3$ in case of GGA functional respectively. But in case of hybrid functional (HSE) computed value of unit volume of pure BTO and Ra-doped materials are 70.89 $Å^3$, 69.83 $Å^3$, 69.44 $Å^3$ and 69.21 $Å^3$ respectively. Concurrently, from table I we can prominently see that the lattice parameters reduce in case of $Ba_{0.75}Ra_{0.25}TiO_3$, $Ba_{0.50}Ra_{0.50}TiO_3$ and $Ba_{0.25}Ra_{0.75}TiO_3$ with favorable addition of doping atoms is excellent agreement with other computed data as well as X-ray diffraction (XRD) (64.384 $Å^3$) results [26]. We asserted that there is no theoretical or experimental support for the existence of current doped atoms in the literature. Future measurements will validate the data we calculated. It is discovered that the lattice parameters in the optimized geometry of (Ra^{+2})-doping at the Ba^{+2} site in $BaTiO_3$ differ somewhat from those of pure BaTiO3. After (Ra^{+2})-doping, the cubic crystalline structure is distorted, leading to this variance. Our data show that the lattice parameters (a, c) and volume of $Ba_{0.75}Ra_{0.25}TiO_3$, $Ba_{0.50}Ra_{0.50}TiO_3$ and $Ba_{0.25}Ra_{0.75}TiO_3$-doped atoms are slightly smaller by (~3 %) than that of pure $BaTiO_3$. The bond length between atoms is excellent to calculate the symmetry of the BTO material structure. The computed Mullikan charge and bond length (Ba–O), (Ti–O) and (Ba–Ti) as well as the tolerance factor are shown in Table 2. The tolerance factors are computed by the following expression

$$t = \frac{0.707(X - O)}{(T_i - O)} \tag{2}$$

The current computed value of the pure and doped- $Ba_{0.75}Ra_{0.25}TiO_3$, $Ba_{0.50}Ra_{0.50}TiO_3$ and $Ba_{0.25}Ra_{0.75}TiO_3$ materials is calculated in the specific range from 0.95 to 1.05 for a cubic perovskite family. Under this suitable range data justifies the reliability of the investigated calculations. BaTiO3 is a compound composed of barium (Ba), titanium (Ti), and oxygen (O). The Mulliken charge refers to the partial charge distribution on each atom within a molecule or compound. The computed effective values for pure (BTO) and doped (Ra) materials are noted 0.73, 3.04, −2.74 and 1.28 respectively. The relaxed Ba–O, Ti–O and Ra–O bonds length of pristine $BaTiO_3$ are 2.91 Å, 2.007 Å, 2.79 Å and 2.80 Å, which are in good similarity with the experimental results. Doping at Ba sites the process decreases the (Ba–O) and (Ti–O) bond lengths because of the lattice distortion. The bond length of oxygen (O) in $BaTiO_3$ (barium titanate) can vary depending on the specific crystal structure and conditions. In the cubic system, the oxygen atoms are

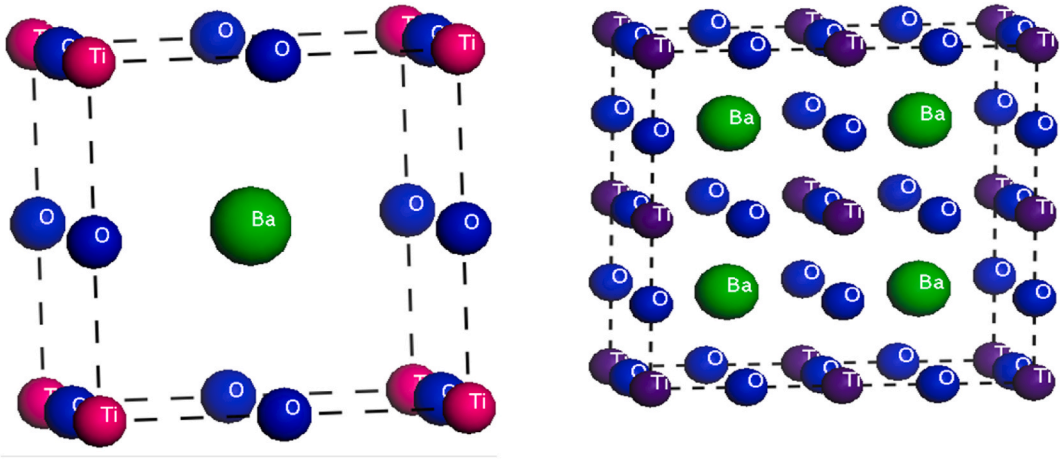

Fig. 1. Optimized structures of: (a) Unit cell $BaTiO_3$, (b) 2 × 2 × 1 supercell.

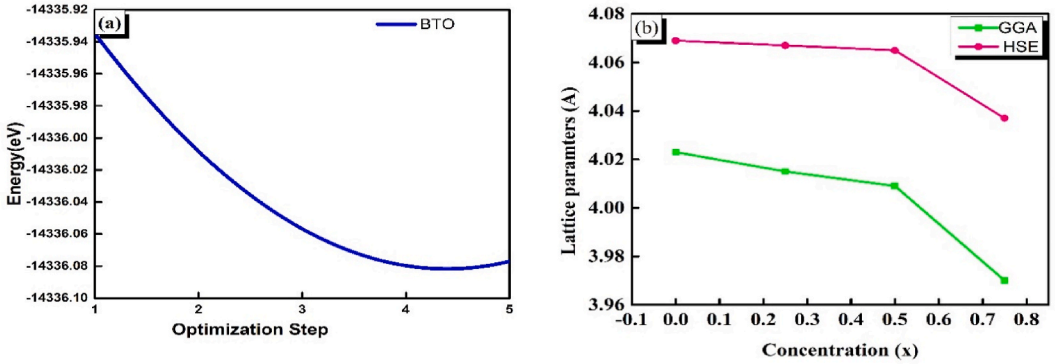

Fig. 2. Optimized curve of $BaTiO_3$ (a) Total energy, (b) Lattice Parameters (Å).

Table 1
The unit cell volume with to geometry optimization parameters of pure and doped-$Ba_{0.75}Ra_{0.25}TiO_3$, $Ba_{0.50}Ra_{0.50}TiO_3$ and $Ba_{0.25}Ra_{0.75}TiO_3$ atoms with additional theoretical and experimental evidence.

Materials	Lattice Parameters(Å)				Band Gap
	a	b	c	Volume(Å^3)	
Experimental Result (BTO) [26]	4.00	4.00	4.024	64.384	3.20eV [27,28]
Theoretical result pure(GGA) [29]	4.007	4.007	4.186	67.211	1.770eV 1.63eV [30]
Calculated Result (GGA BTO)	4.023	4.023	4.167	67.44	1.87eV
$Ba_{0.75}Ra_{0.25}TiO_3$	4.015	4.015	4.147	66.85	1.69eV
$Ba_{0.50}Ra_{0.50}TiO_3$	4.009	4.009	4.095	65.82	1.603eV
$Ba_{0.25}Ra_{0.75}TiO_3$	3.97	3.97	4.178	65.85	1.48eV
Theoretical result BTO (HSE) [31]	4.067	4.067	4.308	71.26	3.25 [32], 3.20eV [33], 3.3eV [34], 3.2 [35]
Calculated Result (HSE BTO)	4.065	4.065	4.290	70.89	3.29
$Ba_{0.75}Ra_{0.25}TiO_3$	4.037	4.037	4.285	69.83	3.25
$Ba_{0.50}Ra_{0.50}TiO_3$	4.008	4.008	4.323	69.44	2.86
$dBa_{0.25}Ra_{0.75}TiO_3$	4.003	4.003	4.319	69.21	2.73

Table 2
Mullikan charge, bond Length and tolerance factors of pure and doped-$Ba_{0.75}Ra_{0.25}TiO_3$, $Ba_{0.50}Ra_{0.50}TiO_3$ and $Ba_{0.25}Ra_{0.75}TiO_3$.

Species	s	p	d	Charge	Bonds	Population	Bond length	Effective Valence	Tolerance Factor
Ba	1.84	4.90	0.68	1.27	O–Ba	0.35	2.91	0.73	0.999 [36]
Ti	2.35	6.59	2.11	0.96	O–Ti	0.47	2.007	3.04	0.785
O	1.84	4.90	0	−0.74	O–O	−0.03	2.79	−2.74	0.737
Ra	2.19	5.97	1.12	0.72	O–Ra	0.02	2.80	1.28	0.690

obtained at the corners of the unit cell, forming oxygen octahedral around the titanium (Ti) atoms. In the cubic phase of BaTiO3, the link between the oxygen and titanium atoms is roughly 1.96 (angstroms) long [37]. However, during the phase transition to the tetragonal phase, the bond lengths can change. In the tetragonal phase, the oxygen atoms still form octahedra around the titanium atoms, but the unit cell becomes distorted, resulting in different bond lengths. The exact value of the oxygen bond length in the tetragonal phase of $BaTiO_3$ would depend on the specific temperature, pressure, and other factors. It's important to note that the bond lengths can also be influenced by factors such as defects, impurities, and lattice strains. Experimental techniques like X-ray diffraction or neutron diffraction can be used to determine the precise bond lengths in a given sample of $BaTiO_3$. Current computes obtain that $Ba_{0.75}Ra_{0.25}TiO_3$, $Ba_{0.50}Ra_{0.50}TiO_3$ and $Ba_{0.25}Ra_{0.75}TiO_3$ doping has large effect on the crystal structure in which all inter atomic bond lengths are modified.

1.3. Electronic properties

Electronic properties refer to the characteristics and behaviors of electrons within a material or system. These properties are crucial for understanding and manipulating electronic devices, such as transistors, diodes, and integrated circuits [38]. Here are some high-level terms related to electronic properties. The ability of a material to carry electric current is referred to as conductivity. According on their conductivity, materials can be classified as conductors, semiconductors, or insulators. Band structure describes the distribution of electron energy levels, known as bands, in a material. The band structure determines the material's electrical

conductivity and optical properties. Fermi level, represents the greatest occupied energy level in a substance at absolute zero. It is vital in establishing the boundary between filled and empty electron states as well as the electrical behaviour of a material. Mobile carriers relate to how easily charge carriers—either electrons or holes—move through a substance when an electric field is present. It is ideal for efficient electronic equipment to have high carrier mobility. The term "energy bandgap" describes the energy difference between a material's valence band, which is its highest occupied energy band and conduction band, which is its lowest unoccupied energy band. It establishes whether a substance exhibits conductor, semiconductor, or insulator behaviour. The deliberate introduction of impurities into a semiconductor material to modify its electrical properties. Doping can create excess electrons (n-type) or holes (p-type) to enhance conductivity [39]. Quantum confinement, occurs when the dimensions of a material are comparable to the wavelength of the electrons. Quantum confinement leads to size-dependent electronic properties, such as discrete energy levels and altered optical properties [40]. These terms provide a glimpse into the vast and intricate field of electronic properties, which plays a fundamental role in the development of modern electronic devices and technologies [41]. The computed electronic band gap of pure and $Ba_{0.75}Ra_{0.25}TiO_3$, $Ba_{0.50}Ra_{0.50}TiO_3$ and $Ba_{0.25}Ra_{0.75}TiO_3$ doped materials as shown in Fig. 3.

Fig. 3(a–d) calculated band gaps of pure BTO and $Ba_{0.75}Ra_{0.25}TiO_3$, $Ba_{0.50}Ra_{0.50}TiO_3$ and $Ba_{0.25}Ra_{0.75}TiO3$ the impurities replaced by Ba^{+2} atoms with GGA functional respectively. The calculated band gap before and after $Ba_{0.75}Ra_{0.25}TiO_3$, $Ba_{0.50}Ra_{0.50}TiO_3$ and $Ba_{0.25}Ra_{0.75}TiO_3$ doped with Ba^{+2} sides are 1.87eV, 1.69eV, 1.603eV and 1.48eV respectively. We understood that the appropriate addition of Ra^{+2} impurities causes the extremely low energy level as well as the CB of the crystal structure to shift more shift in the direction of low energy ranges and narrows the band gap. This result causes the A-site (Ba^{+2}) atom's electro negative to have a significant impact on the electronic band gap and the CB's state hybridization to grow, which facilitates the free electrons' easy travel along the wall. The calculated band gap is an indirect, optically inactive response band with highest value of VB observed at symmetry points of (X-G-X) and minimum value of CB found at symmetry points of (X-G). After doping $Ba_{0.75}Ra_{0.25}TiO_3$, $Ba_{0.50}Ra_{0.50}TiO_3$ and

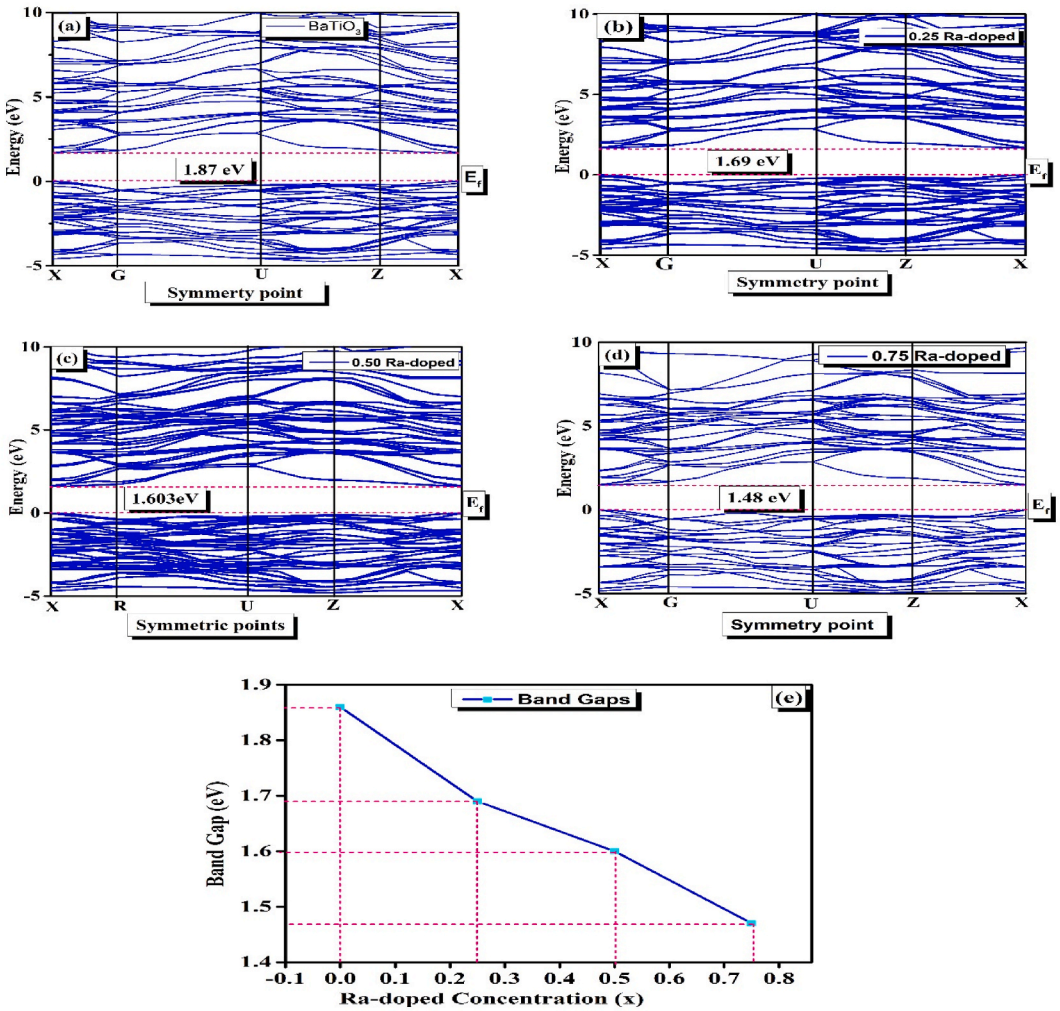

Fig. 3. Band structures with GGA of (a) Pure BTO (b) $Pb_{0.75}Ra_{0.25}TiO_3$ (c) $Ba_{0.50}Ra_{0.50}TiO_3$ and (d) $Ba_{0.25}Ra_{0.75}TiO_3$, (e) Trends of Band gaps of pure BTO and (Ra) doped.

$Ba_{0.25}Ra_{0.75}TiO_3$, the highest value of VBs is observed at low symmetry points (X-X), and the lowest value of CBs is recognized at high symmetry points (G-X), and the band gaps change from being indirect to being direct and become optically active. With increasing doping concentration (x) at the A-site, the band gap trends of pure BTO and (Ra)-doped materials are continually decreasing, according to Fig. 3(e). According to calculations in Fig. 4(a–d), the electronic band gaps of pure (BTO) and doped materials with hybrid functionals (HSE) made of $Ba_{0.75}Ra_{0.25}TiO_3$, $Ba_{0.50}Ra_{0.50}TiO_3$ and $Ba_{0.25}Ra_{0.75}TiO_3$ are, respectively, 3.29eV, 3.25eV, 2.86eV, and 2.73eV as well as good comparable with experimental (3.20) and theoretical (3.25) reported data. The band gap trends of both pure and doped materials are comprehensively addressed in Fig. 4(e). Additionally, when compared to band gap curves of crystals without doping, we discovered that the band gap very minimally changes when the Ba^{+2} site atoms in $Ba_{0.75}Ra_{0.25}TiO_3$, $Ba_{0.50}Ra_{0.50}TiO_3$ and $Ba_{0.25}Ra_{0.75}TiO_3$ are doped. The bands divide as a result of mobile electron transitions from VB to CB, leading to a high number of states in the doped system. Additionally, doped atoms (Ra) enlarge the BTO gap and shorten the band gap. This effect on band gap makes it simple to archive mobile electrons in the D-state of (Ra). The band gap is less because the Fermi surface may shift closer to the VB as the mobile electron impurity decreases. The coupling effect of Ti-3d of Ra-3p and Ba-5p of O-2p, as well as various concentration levels obtained within the band gap, cause the band gap to widen after (Ra) doped materials concentrations are replaced by (Ba) sites. Additionally, the atomic radii increase with increasing atomic number in a system, weakening the strength of the outermost mobile electrons. The outcome is a reduced electronegativity and a bigger band gap for (Ba^{+2})-site impurities. The electronegativity of impurity atoms' ion radius and charge is often what causes the band gap to alter. After discussed computed electronic band structure, we explained the TPDOS and EPDOS as well as TDOS of pure BTO and $Ba_{0.75}Ra_{0.25}TiO_3$, $Ba_{0.50}Ra_{0.50}TiO_3$ and $Ba_{0.25}Ra_{0.75}TiO_3$ doped materials as shown in Fig. 5.

The partial density of states (PDOS) characterizes the contribution of each atomic site or orbital to the total density of states. It

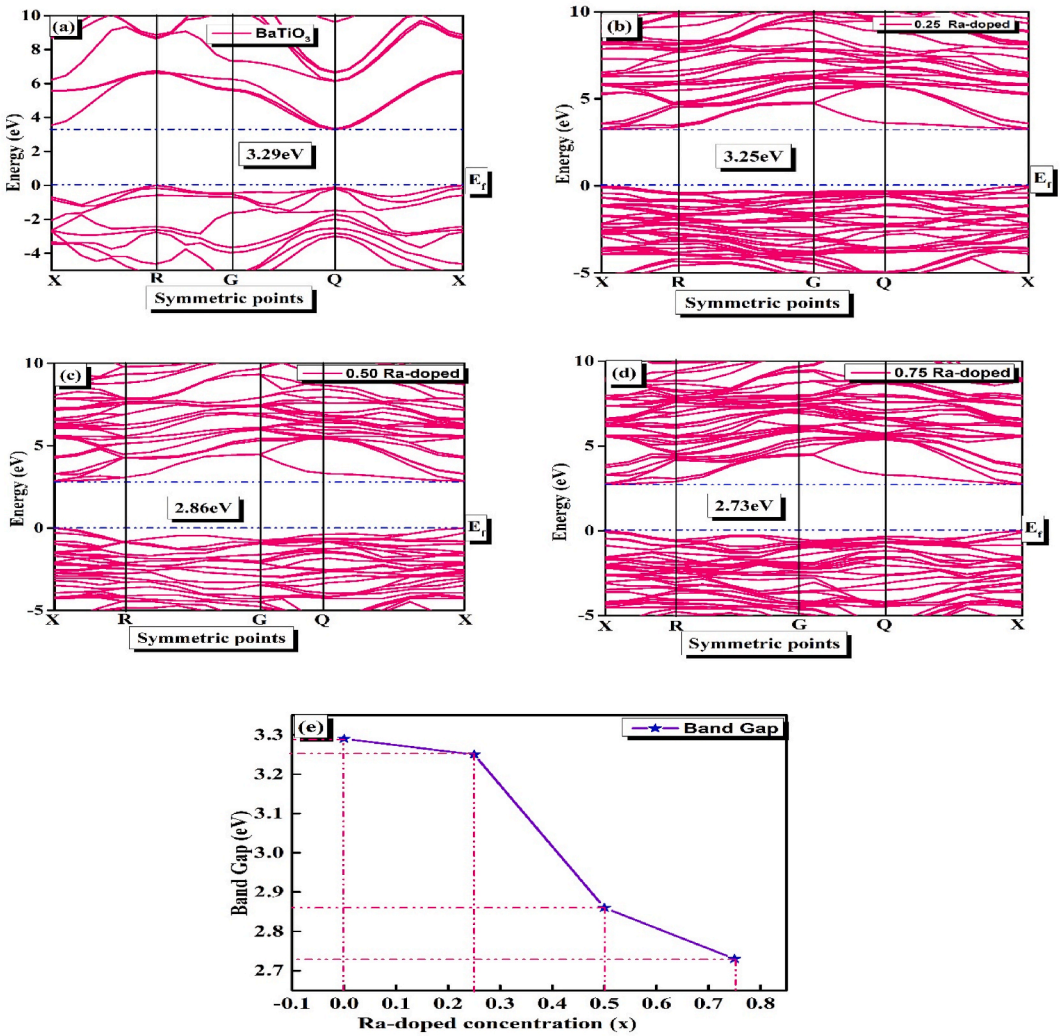

Fig. 4. Band structures with HSE of (a) Pure BTO (b) $Ba_{0.75}Ra_{0.25}TiO_3$ (c) $Ba_{0.50}Ra_{0.50}TiO_3$ and (d) $Ba_{0.25}Ra_{0.75}TiO_3$, (e) Trends of Band gaps of pure BTO and (Ra) doped.

breaks down the TDOS into individual components, allowing the analysis of the electronic structure at a more localized level. The PDOS provides information about the energy levels available at specific atomic sites or within specific energy ranges. To calculate the total density of states, you would typically sum up the contributions from all the partial density of states for each atom or orbital in the system. This summation gives the overall distribution of electronic states across the energy spectrum. The total partial density of states is not a standard term in the field and seems to combine conflicting ideas. However, you can calculate the total density of states by summing up the contributions from individual partial densities of states. Fig. 5 (a) computed curve of pure (BTO) and $Ba_{0.75}Ra_{0.25}TiO_3$, $Ba_{0.50}Ra_{0.50}TiO_3$ and $Ba_{0.25}Ra_{0.75}TiO_3$ doped system. The total partial density of states (TPDOS) the three prominent contribution peaks are noted 26.27 (BTO-p), 19.16 (BTO-d) and 5.85 (BTO-p) states at energy ranges are −0.74eV, 3.65eV and 14.37eV respectively. Due to the fast movement of free electrons the remarkable peaks shifted at −4.61eV–0.53eV. Fig. 5 (b) computed the (Ba)

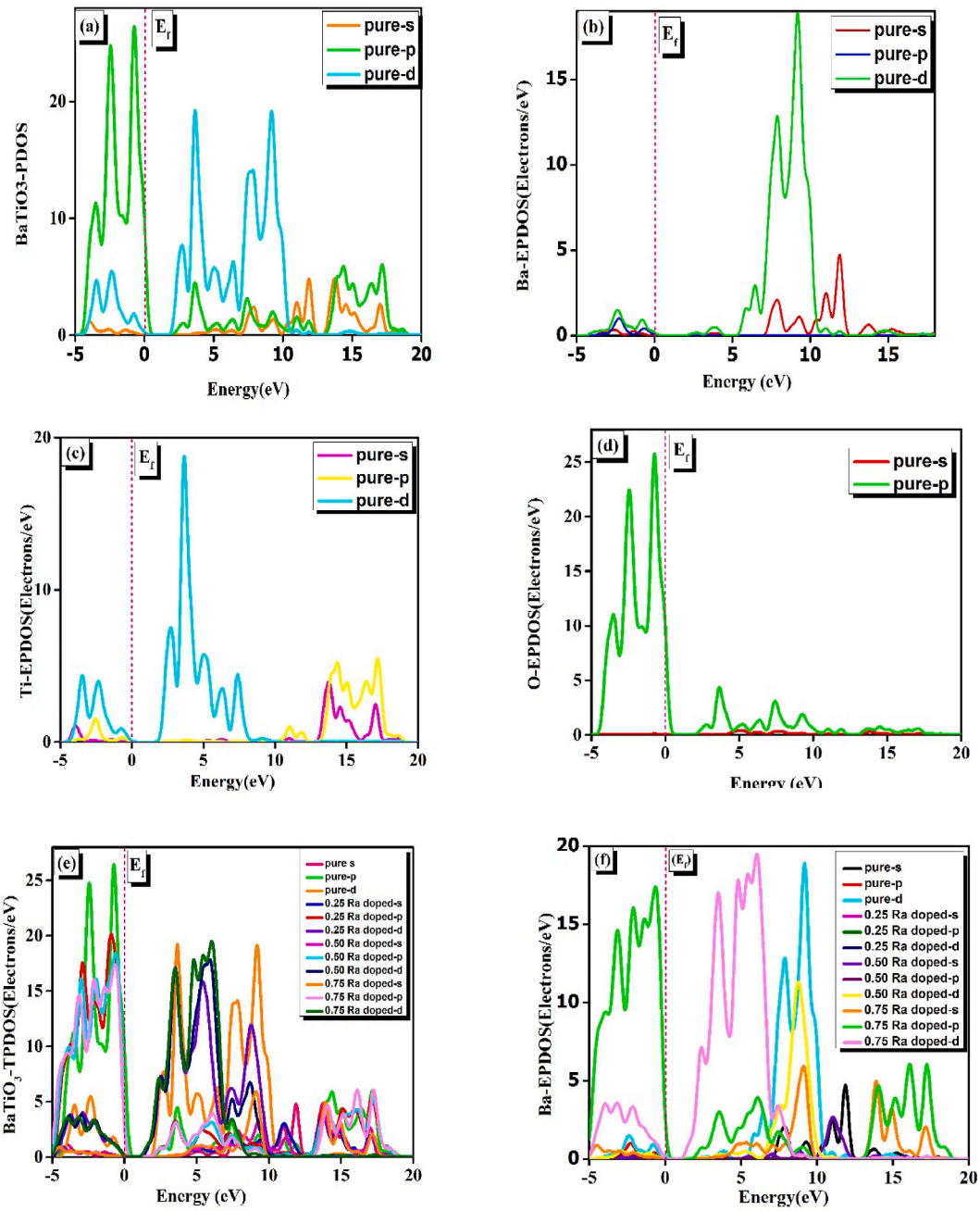

Fig. 5. (a) PDOS of $BaTiO_3$ (b) EPDOS of Ba (c) EPDOS of Ti (d) EPDOS of O (e) TPDOS of $BaTiO_3$ (f) TEPDOS of Ba, (g) TEPDOS of Ti, (h) TEPDOS of O, (i) EPDOS of Ra and (j) TDOS

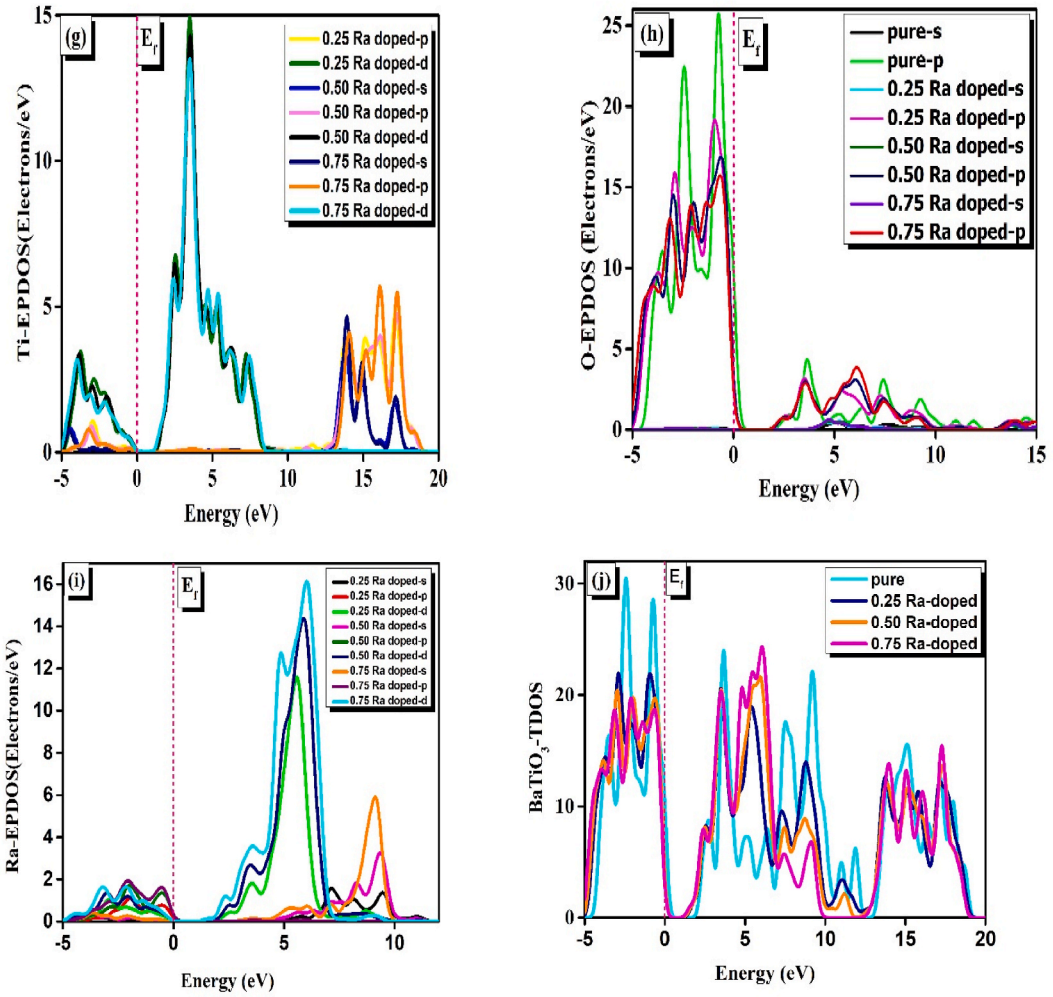

Fig. 5. (*continued*).

Elemental partial density of states (EPDOS), the valuable three peaks are found 18.82 (BTO-d), 4.65 (BTO-s) 3.99 (0.25Ra-p) states at energy ranges noted are 9.22, 11.88 and 17.75 respectively. Fig. 5 (c, d) computed the curves of Ti and O (EPDOS), in this case the three prominent peaks are noted 18.66 (BTO-d), 5.14 (BTO-p), 5.38 (0.50Ra-p), 25.59 (BTO-p), 4.29 (BTO-s) and 2.95 (0.75Ra-p) at energy ranges are noted 3.65eV, 14.32eV, 17.16eV, −0.74eV, 3.66eV and 7.43eV respectively. The very fast moving free electrons from VB to CB the edges shifted from 1.65eV to 9.73eV and −4.66eV–0.57eV. We found that the atomic states (Ti-3d), (Ba-6s), (Ba-3p), and (O-2p) all strongly contribute to the Fermi level. The extraordinary contribution of Ti atoms in the (3d) and (3p) states indicates that they play a more significant role close to the Fermi level E_f. When Ba0.75Ra0.25TiO3, Ba0.50Ra0.50TiO3, and Ba0.25Ra0.75TiO3 are added to BTO, significant new PDOS edges are produced in the energy range of around −5 eV–2 eV, and the influence on the TDOS as a whole is transferred to the lower energy range. Ra-atoms contribute significantly to the TDOS close to the Fermi level in the 3p and 3d states. The TPDOS peaks of (Ti-3d) are steadily refrained when the doping impurities increase from (0–0.75). Calculated TPDOS curves for the pure (BTO) and doped systems with $Ba_{0.75}Ra_{0.25}TiO_3$, $Ba_{0.50}Ra_{0.50}TiO_3$ and $Ba_{0.25}Ra_{0.75}TiO_3$ doped are shown in Fig. 5 (e). The three conspicuous maximum peaks produced by the useful transition of free electrons are 26.46 (BTO-5p), 19.19 (BTO-3d), and 19.66 (0.75Ra-3p) states in energy ranges of 0.69 eV, 3.71 eV, and 6.21 eV, respectively. The outstanding edges moved from −4.5eV to 0.43eV during the transition of swiftly moving free electrons from VB to CB. The three greatest peaks generated around the fermi level are 19.48 (0.75Ra-3d), 18.90 (BTO-3d), and 6.01 (0.75Ra-5p) states at 6.05eV, 9.24eV, and 16.24eV, respectively. Fig. 5 (f, g) calculated the curves of Ba and Ti TEPDOS for (BTO) and (Ra) doped materials. When the VB electrons obtain additional energy, they move quickly from the VB to the CB, shifting their prominent edges from 1.16 eV to 9.69 eV. The highest contribution peaks for Ti-TEPDOS have been identified as 14.89 (0.25Ra-3d), 4.50 (0.75Ra-6s), and 5.35 (0.75Ra-5s) states, which are located at 3.51eV, 13.94eV, and 16.13eV energy ranges, respectively. The maximum edges changed from 1.35 eV to 8.31 eV around the Fermi level. The primary three notable contribution peaks are 25.45 (BTO-5p), 4.11 (BTO-3p), and 3.80 (0.75Ra-5p) states at energy ranges are marked as −0.73eV, 3.65eV, and 6.11eV in Fig. 4(h), which computed the curve of O-TEPDOS of pure and doped materials. When the doping impact on BTO was calculated, the Ra-EPDOS created several impressive peaks. At energy ranges of 6.01 and 7.47, 16.06 (0.75Ra-3d)

and 5.84 (0.75Ra-6s) states are found. Doping has resulted in a maximum state hybridization near the Fermi energy level under interactions between 3d states of $Ba_{0.75}Ra_{0.25}TiO_3$, $Ba_{0.50}Ra_{0.50}TiO_3$ and $Ba_{0.25}Ra_{0.75}TiO_3$ doped atoms, and 5p, 6s interactions between these 3d states and the 2p orbital of O atoms. Additionally, the conductivity has been enhanced by the carrier's transition near the Fermi energy level. Fig. 5 (j) computed the TDOS of pure and $Ba_{0.75}Ra_{0.25}TiO_3$, $Ba_{0.50}Ra_{0.50}TiO_3$ and $Ba_{0.25}Ra_{0.75}TiO_3$ doped atoms concentrations. Below fermi level referred as the upper part of VB (ranges from -5eV to 0eV), O-2p states has major contribution than Ba-5p states. Hence, Ti-3d states has maximum peak than 6s and 5p states of Ba above the fermi level referred as CB at the energy range from −4.65eV to 0.57eV. In case of $Ba_{0.75}Ra_{0.25}TiO_3$, $Ba_{0.50}Ra_{0.50}TiO_3$ and $Ba_{0.25}Ra_{0.75}TiO_3$ impurities, from curve we can conclude that in each case of (Ra) doping, the 5p-state is prominent for all concentrations of doping in VB, which is considered below the fermi level at energy range from -5eV to 0.5eV. The other states have small contribution rather than these states. The 3d states have major contribution for all concentration of $Ba_{0.75}Ra_{0.25}TiO_3$, $Ba_{0.50}Ra_{0.50}TiO_3$ and $Ba_{0.25}Ra_{0.75}TiO_3$ atoms in CB assumed above the fermi level at energy range from 6.05eV to 14.37eV. Additionally, incorporation of impurities such as $Ba_{0.75}Ra_{0.25}TiO_3$, $Ba_{0.50}Ra_{0.50}TiO_3$ and $Ba_{0.25}Ra_{0.75}TiO_3$ atoms in pure BTO, the dissimilitude in CB and VB can be exactly identified by curves. In the scenario of doping of $Ba_{0.75}Ra_{0.25}TiO_3$, $Ba_{0.50}Ra_{0.50}TiO_3$ and $Ba_{0.25}Ra_{0.75}TiO_3$ atoms in pure material overall strong O-2p state is more eminent in (Ra) doped BTO due to which VB crosses the fermi level, as it is also observed in band gap curves within the energy range from -5eV to 0eV. The CB after the doping of $Ba_{0.75}Ra_{0.25}TiO_3$, $Ba_{0.50}Ra_{0.50}TiO_3$ atoms the 3d state of Ti, 3p state of Ba and 3p state of Ra respectively has strong appearance in contrast of Ba-3p states. Moreover, in case of $Ba_{0.25}Ra_{0.75}TiO_3$ doping 3d state of Ti and Ra predominant contribution relative to the Ba-3p states the Ra-3p states in the energy range of 6.5eV–11eV.

1.4. Formation energy

The formation energy of a compound is the energy change associated with the formation of that compound from its constituent elements [42]. In the case of BaTiO3 (barium titanate), the formation energy can be computed by considering the (H) energies of formation of its constituent elements and applying Hess's law [43]. The balanced equation for the formation energy of $BaTiO_3$ can be written as follows:

$$Ba + Ti + 3/2\ O_2 \rightarrow BaTiO_3 \quad (3)$$

To calculate the formation energy, you need to know the enthalpies of formation of $BaTiO_3$, Ba, Ti, and O_2. The enthalpy of

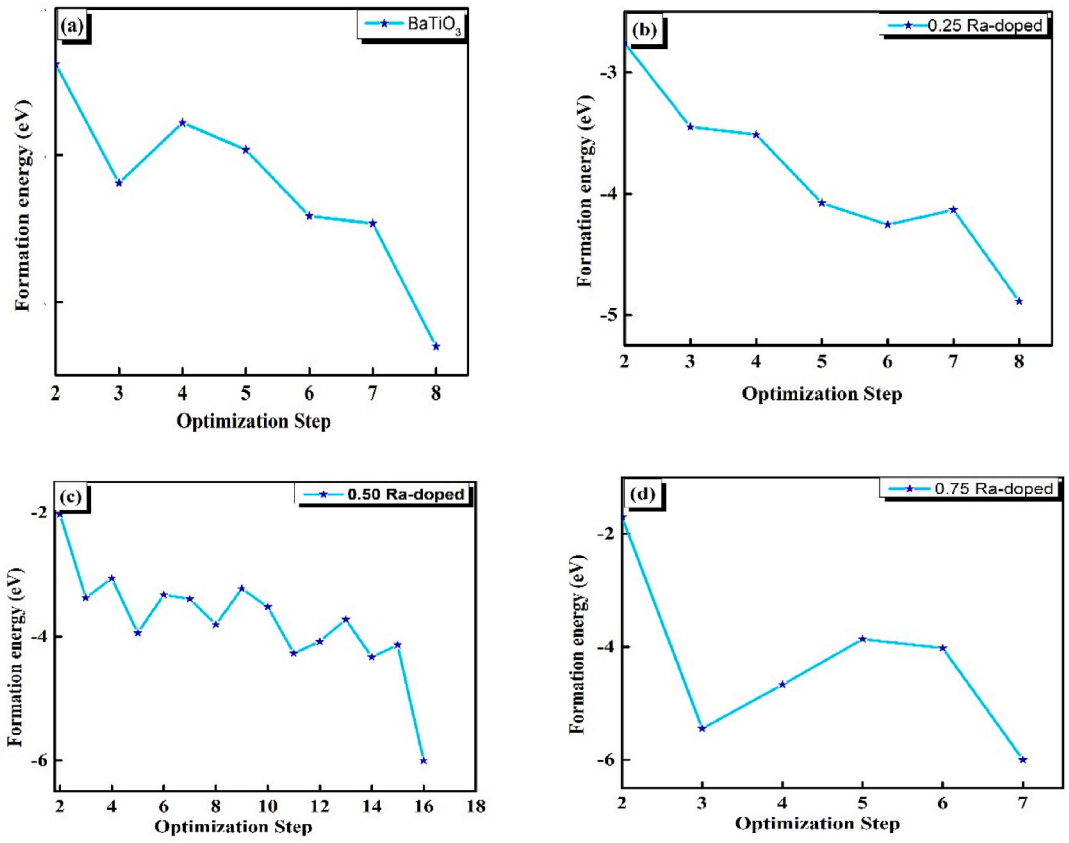

Fig. 6. Formation energy of (a) Pure BTO (b) $Ba_{0.75}Ra_{0.25}TiO_3$ (c) $Ba_{0.50}Ra_{0.50}TiO_3$ and (d) $Ba_{0.25}Ra_{0.75}TiO_3$.

formation values can vary depending on the source and the specific conditions. The standard enthalpy of formation of $BaTiO_3$ is around −2140 kJ/mol. The standard enthalpy of formation of Ba is approximately 0 kJ/mol since it is considered as the reference state. The standard enthalpy of formation of Ti is around 0 kJ/mol in its most stable form (Ti-solid). The standard enthalpy of formation of O_2 (gas) is approximately 0 kJ/mol in its standard state. Using these values, you can calculate the approximate formation energy of $BaTiO_3$. The main concept of formation energy is the energy achieved when Ra atoms replaced with other atoms of concentrations. According to expressions of $Ba_{0.75}Ra_{0.25}TiO_3$, $Ba_{0.50}Ra_{0.50}TiO_3$ doping formation energy are as follows

$$E_f\ (Ra\rightarrow Ba) = E\ (Ra\rightarrow Ba) - E(BaTiO_3) + \mu_{Ba} - \mu_{Ra} \tag{4}$$

$$E_f\ (Ra \rightarrow Ti) = E\ (Ra \rightarrow Ti) - E(BaTiO_3) + \mu_{Ti} - \mu_{Ra} \tag{5}$$

E (Ra→ Ba) and E (Ra→ Ti) are the energy values after the (Ra) atoms changes with Ba or Ti atoms in (BTO) through system optimization. E (BTO) is the energy of the un-doped system and μ_{Ra} is called the potentials of Ra-doped for each atoms in the BTO. The formation energies of $Ba_{0.75}Ra_{0.25}TiO_3$, $Ba_{0.50}Ra_{0.50}TiO_3$ and $Ba_{0.25}Ra_{0.75}TiO_3$ doped (Ra^{+2}) replaced with Ba site in BTO are computed as follows in Fig. 5.

We discovered that the more (E_f) is less, the more stable the BTO system. Fig. 6 (a to d), the computed Formation energy with and without doping systems. The stability of the Ba-site doping attained in the doped (BTO) system is Ra0.25 > Ra0.50 > Ra0.75 in that order. Additionally, study shows that the (E_f) of Ra energy decreases when the radius and charge between Ra-doped atoms increases [44]. This justifies that the experimental computation data are dependable with the general rule that it is easier to change an atom with atom with a similar ionic radius. Keep in mind that actual values might vary, and it is always recommended to consult reliable sources or perform more accurate calculations using updated data if precision is important for target application [45].

1.5. Elastic and mechanical properties

Barium titanate ($BaTiO_3$) is a well-known ferroelectric material that exhibits a combination of elastic and mechanical properties [46]. Here are some key characteristics of $BaTiO_3$. $BaTiO_3$ has three main elastic constants that describe its mechanical behavior. $BaTiO_3$ has a relatively high Young's modulus, which is a measure of its stiffness or resistance to deformation under applied stress [47]. Shear modulus (G), also has a significant shear modulus, which represents its resistance to shear deformation. Poisson's ratio (ν), typically exhibits a Poisson's ratio close to 0.3, indicating that it contracts laterally when subjected to axial tensile stress [48]. $BaTiO_3$ is primarily known for its ferroelectric behavior, which means it can exhibit spontaneous polarization when an external electric field is applied. This property makes $BaTiO_3$ useful in various applications, such as capacitors, actuators, and sensors. $BaTiO_3$ undergoes phase transitions at specific temperatures [49]. As the temperature increases, it goes through a series of phase transitions, including the cubic phase ($Pm^{-}3m$) at around 120 °C and the tetragonal phase) at approximately 130 °C [50]. $BaTiO_3$ has a high dielectric constant, making it suitable for applications in energy storage and electronic devices. The dielectric constant of $BaTiO_3$ varies depending on factors such as temperature, frequency, and the presence of impurities [51]. The total energy of the cubic crystal system in strained states is used by following expression.

$$E_{total} = E^{x}_{total} + (V_{strained} - V_{unstrained}) \tag{8}$$

Here, (E^{x}_{total}) and ($V_{unstrained}$) are denoted by the total energy and volume of unstrained system and ($V_{strained}$) is volume of strained (BTO) system and P is the pressure as well as (φ_l) is elastic energy of the system defined as

$$P = -\partial {E_{total}}^{x} / \partial V) \tag{9}$$

$$\text{Or } (\varphi_l) = \left(\frac{V_{strained}}{2} C_{ijkl}\varepsilon_{ij}\varepsilon_{kl}\right) \tag{10}$$

where i, j k, and l are called demi-indices its values states from (1, 2, 3, … … … ….)

Moreover, the elastic energy is improved in Voigt two further notations following as:

$$(\varphi_l) = \left(\frac{V_{strained}}{2} C_{ij}\varepsilon_i\varepsilon_j\right) \tag{6}$$

The notation C_{ij} are called elastic moduli,

$$\text{So } C_{ij} = \left(\frac{1}{V_{untrained}} \frac{\partial^2 E_{total}}{\partial_{\varepsilon_i}\partial_{\varepsilon_j}}\right) \tag{7}$$

It's important to note that the values of these elastic constants can vary depending on the specific cubic crystal structure and the material being considered [52]. Different materials have different values for C_{11}, C_{12}, and C_{44} [53]. The bulk modulus, as well as shear modulus using the Voight technique, are given by

$$B_H = \frac{(C_{11} + 2C_{12})}{3} \tag{11}$$

$$G_H = \frac{(G_V + G_R)}{2} \tag{12}$$

$$G_V = \frac{(C_{11} - C_{12} + 3C_{44})}{5} \tag{13}$$

$$G_R = \frac{5[(C_{11} - C_{12})C_{44}]}{[4C_{44} + 3(C_{11} - C_{12})]} \tag{14}$$

where B_R and G_R are called Reus's bulk and shear modulus, corresponding to the Voigt approximation. By using this technique, we calculate the young modulus, shear modulus, and Poisson ratios of perovskite ferroelectric materials like BTO under different pressure conditions.

$$E = \frac{9GB}{3B + G} \tag{15}$$

$$A = \frac{2C_{44}}{C_{11} - C_{12}}, \tag{16}$$

A is called anisotropy factor. Computed value of Poisson ratio (σ) by the following relations.

$$\sigma = (3B\text{-}2G)/2(3B\text{-}G) \tag{18}$$

The G_v Voigt's shear modulus with respect to upper bond of (G) values and G_R is denoted by Reuses modulus with respect to lower bond of (G) values [54]. This expression can be denoted by

$$G_v = \left(\frac{C_{11} - C_{12} + 3C_{44}}{5}\right) \tag{19}$$

$$\xi = \left[\frac{C_{11} + 8C_{12}}{7C_{11} + 2C_{12}}\right] \tag{17}$$

To sustain the mechanical stability that clarifies the description of the crystal systems and set of elastic parameters is achieved from the reasonable change in elastic deformation due to the elastic constant C_{ij} is computed with the total energy technique and unit cell exposed the number of limited size strains along dispersed strain direction [55]. The computed elastic and mechanical parameters are in the following Table 3.

Young modulus, bulk modulus, poison ratio, and sheer modulus are computed as mechanical reactions that are significant physical responses, especially for engineering applications. The degree of anisotropy in the crystal structure is determined by excellent anisotropy. The value of A = 1 indicates that the hardness of the polycrystalline crystal and the total isotropy anisotropy in the crystal structure are estimated by computing the key parameters. These equations are used to determine hardness [58]. The Ra-doped materials' resistance to changes in volume and elastic constant are determined by the bulk modulus and shear modulus, respectively. The Poisson ratio is formed by computing the values of the young modulus stiffer in material and the degree of directionality of the covalent bond, as shown in Table 3. One of the two key concepts for understanding these compounds with anisotropy values higher than or equal to one is the elastically anisotropic response. Table 3 displays the computed elastic and mechanical parameters, including the bulk, shear, young's, and Poisson ratios. In the above table, the computed values of Young's modulus, Klienman coefficients, bulk modulus, and shear modulus of pure (BTO) material values are 145.94, 104.432, 252.96 and −0.28 respectively. However, the values found for the doped Ba0.75Ra0.25TiO3, Ba0.50Ra0.50TiO3, and Ba0.25Ra0.75TiO3 materials are 154.37, 97.84, 242.34, −0.23, 168.63, 95.43, 240.19, −0.25, and 164.56, 90.79, 104.031 and −0.26 (0.75Ra), respectively. According to our computed results, when the doping concentration (x) increases, the values of the bulk modulus are continuously improved while the values of the shear modulus drop. However, in the case of the Young modulus, the calculated values and Klienman coefficients drop along with rising doping concentrations. If the calculated greater Young modulus (E) value for pure BTO and Ba0.75Ra0.25TiO3, Ba0.50Ra0.50TiO3, and Ba0.25Ra0.75TiO3-doped materials justified that these compounds' nature is hard and broken [33]. The harness of a compound

Table 3
Shows the calculated elastic and mechanical values of pure and $Ba_{0.75}Ra_{0.25}TiO_3$, $Ba_{0.50}Ra_{0.50}TiO_3$ and $Ba_{0.25}Ra_{0.75}TiO_3$.

Coefficients	C_{11} (GPa)	C_{12} (GPa)	C_{44} (GPa)	B (GPa)	A	G (GPa)	E (GPa)	B/G	σ	ξ
Experimental values ($BaTiO_3$) [56,57]	307	112	48							
	305	106	128							
Theoretical values [36,57]	295	100	116	245.40	1.32	116.99	302.85	0.48	0.29	
	377.36	179.43	130.83							
Current values $BaTiO_3$	240.76	97.066	125.73	145.94	1.38	104.43	252.96	0.57	0.21	−0.28
$Ba_{0.75}Ra_{0.25}TiO_3$	268.69	93.13	107.44	154.37	1.22	97.84	242.34	0.63	0.23	−0.23
$Ba_{0.50}Ra_{0.50}TiO_3$	283.50	104.82	105.85	168.63	1.18	95.43	240.19	0.77	0.23	−0.25
$Ba_{0.25}Ra_{0.75}TiO_3$	285.09	106.26	92.97	164.56	1.02	90.79	104.03	0.99	0.19	−0.26

can also direct linked in terms of shear modulus (G). Its elastically isotropic nature is indicated if it has a value less than A <1 [59]. The computed values of A in case of BTO and $Ba_{0.75}Ra_{0.25}TiO_3$, $Ba_{0.50}Ra_{0.50}TiO_3$ and $Ba_{0.25}Ra_{0.75}TiO_3$ are 1.38 (BTO), 1.22 (0.25Ra), 1.18 (0.50 Ra) and 1.02 (0.75Ra) respectively. The computed data clearly shown that in case of pure and Ra-doped elastically anisotropic nature. According to the aforementioned equation, the calculated data of A in cases of the calculated in-plane stiffness of Ra-doped of the formation of the additionally obtained by the A and Poisson ratio are in good agreement with the data from the experimentally measured 1.35 (BTO) and theoretically predicted 0.32 (BTO) measurements. The Pugh ratio, also known as the brittleness index or B/G ratio, is a dimensionless parameter that is used to evaluate the brittleness or ductility of a material. It is calculated by dividing the bulk modulus (B) by the shear modulus (G) of the material. In the case of BTO, which is a ferroelectric ceramic material, the Pugh ratio (B/G) provides insights into its mechanical properties. Here's the significance of the Pugh ratio for BTO. The Pugh ratio helps determine whether BTO is more brittle or ductile. A higher Pugh ratio indicates a higher level of brittleness, meaning the material is more likely to fracture when subjected to stress. Conversely, a lower Pugh ratio suggests greater ductility, indicating the material's ability to deform plastically before breaking [60]. The Pugh ratio is also linked to the mechanical stability of BTO. If the Pugh ratio is high, it implies that the material has a lower tolerance for strain and may exhibit lower resistance to mechanical failure. Conversely, a lower value suggests better mechanical stability, indicating that BTO can withstand greater deformations without fracturing. The Pugh ratio can be used as a comparative parameter for material selection. When evaluating different materials for a particular application, engineers often consider the Pugh ratio to assess their brittleness or ductility. BTO with a specific Pugh ratio can be compared with other materials, and a suitable choice can be made based on the desired mechanical properties. It is important to note that the Pugh ratio alone does not provide a comprehensive understanding of the mechanical behavior of $BaTiO_3$. Other mechanical properties, such as tensile strength, fracture toughness, and hardness, should be considered in conjunction with the Pugh ratio to obtain a more complete characterization of the material's mechanical performance. Pugh's ratio (B/G) provide further details on the nature of various materials, helping us to achieve the brightness and ductility of our materials [55]. If a material's Pugh's ratio is more than (B/G > 1.75), it is said to have a ductile nature, and if it is lower (B/G 1.75), it is said to have a brittle nature. Ra-doped materials had estimated B/G values of 0.57 (BTO), 0.63 (0.25Ra), and 0.77 (0.50Ra), respectively. The Ra-doping materials are demonstrated to have ductile character in the case of pure (BTO). The Poisson ratio is a material response that justifies the relationship between the lateral strain and the axial strain of a material when subjected to an external force or stress. For $BaTiO_3$ (Barium Titanate), the Poisson ratio plays a significant role in determining its mechanical and electromechanical behavior. It provides information about the elastic behavior of $BaTiO_3$ and quantifies how the material responds to deformation, particularly in terms of the lateral expansion or contraction that occurs when it is subjected to axial stress. The unique combination of ferroelectric and piezoelectric properties in $BaTiO_3$ makes it highly valuable for various device applications. Its Poisson ratio affects the performance of $BaTiO_3$-based devices, such as actuators, sensors, transducers, and piezoelectric energy harvesters. By manipulating the Poisson ratio, researchers and engineers can optimize the performance and efficiency of these devices. The calculated Poisson ratio (σ) supports the degree of covalent bond directionality for both pure BTO and materials containing $Ba_{0.75}Ra_{0.25}TiO_3$, $Ba_{0.50}Ra_{0.50}TiO_3$ and $Ba_{0.25}Ra_{0.75}TiO_3$ doping. If the computed value of (σ) is low, it will be ($\sigma = 0.1$) for covalent compounds and ($\sigma = 0.25$) for ionic compounds. The nature of the material belongs to the ductile family if the computed value of (σ) is more than or equal to > 0.25, and the brittle family if the computed value of (σ) is less than or equal to 0.25 [61]. At the end we discuss the computed values of Poisson ratio of pure (BTO) and dopant (Ra) materials are 0.21 (BTO), 0.23 (0.25Ra), 0.23 (0.50Ra) and 0.19 (0.75 Ra) respectively. The computed data in cases of (BTO) and Ra-doped (BTO) are shown ductile nature. The Kleinman coefficient (ξ) depend upon the internal strain and also indicates relative ease of bond bending against bond stretching of $Ba_{0.75}Ra_{0.25}TiO_3$, $Ba_{0.50}Ra_{0.50}TiO_3$ and $Ba_{0.25}Ra_{0.75}TiO_3$-doped materials. In stable system, the minimizing bond (Ba–O), (Ba–Ti) and (Ra–O) bending higher than zero ($\xi = 0$) and other hand minimizing these bonds stretching [62] large value to ($\xi = 1$). In current analysis investigated value of (ξ) to be pure BTO is −2.28 and $Ba_{0.75}Ra_{0.25}TiO_3$, $Ba_{0.50}Ra_{0.50}TiO_3$ and $Ba_{0.25}Ra_{0.75}TiO_3$-doped materials are 0.23 (Ra0.25), 0.25 (0.50Ra) and (0.75Ra) respectively. After complete analysis of (ξ), it is clear that (Ra)-doped materials shows slightly large resistance to bond bending as well as bond angle distortion as compare to pure $BaTiO_3$.

2. Optical properties

The optical properties of material can be revealed by exploring its electronic structure using different parameters. The best technique for determining the energy band structure of solid materials is optical analysis. $BaTiO_3$ possesses optical properties like high refractive index, transparency, birefringence, electro-optic effect, and nonlinear optical behavior [63]. These properties make it a versatile material for various optical applications, including waveguides, lenses, modulators, switches, and frequency converters. Optical parameters are complex dielectric function $\varepsilon(\omega)$, absorption $I(\omega)$, refractive index $n(\omega)$, loss function $L(\omega)$, reflectivity $R(\omega)$, extinction coefficient (k) and optical conductivity which illustrate the response of doped material [64]. We can observe that material is auspicious for nanotechnology and Optoelectronic devices from these parameters. When material is exposed to the radiations after interaction the response of the material can be narrated by complex dielectric function which contains two parts real dielectric function $\varepsilon_1(\omega)$ (RDF) and imaginary dielectric function $\varepsilon_2(\omega)$ (IDF) reported in Maxwell's equation [65].

$$\varepsilon(\omega) = \varepsilon_1(\omega) + i\varepsilon_2(\omega) \tag{20}$$

where $\varepsilon_1(\omega)$ depicts the capability of material to store energy and polarization of material. While $\varepsilon_2(\omega)$ narrates the damped oscillation of light and energy dissipation.

$$\varepsilon_1{}^{interband}(\sigma) = 1 + \frac{2}{\pi} p \int_0^{\infty} \frac{\varepsilon_2{}^{interband}(\sigma)\overline{\sigma}}{\overline{\sigma}^2 - \sigma^2 + \eta} d\overline{\sigma} \tag{21}$$

where P is the foremost excellent result and η is represent by an useable notation, the DF for intraband changes $\varepsilon_1{}^{interband}(\sigma)$ was gained by associated with dmde relation for a compulsory plasma frequency (σ_p) and the damping parameter (μ)

$$\varepsilon_1{}^{interband}(\sigma) = 1 - \frac{\sigma_p{}^2}{\sigma_p{}^2 + i\mu\sigma} \tag{22}$$

$$\varepsilon_1{}^{interband}(\sigma) = 1 - \frac{\sigma_p{}^2\tau^2}{1 + \sigma^2\tau^2} \tag{23}$$

$$\varepsilon_2{}^{interband}(\sigma) = \frac{\sigma_p{}^2\tau}{\sigma(1 + \sigma^2\tau^2)} \tag{24}$$

Here, τ is denote by $\mu = 1/\tau$ a relaxation time achieved from a large order calculating and σ_p is the plasmonic frequency calculated by the following relations [66,67],

$$\sigma_p{}^2(x, y) = \frac{-4\pi\tau^2}{\Omega} \sum_{p,i} 2 \frac{\partial\omega_i(E_s)}{\partial E_s} < \frac{E_{ip}}{\partial p}\hat{x} > \frac{E_{ip}}{\partial p}\hat{y} > \tag{25}$$

Once σ_p and τ is justified as the real and complex coefficients of the interbond part of the dielectric function.

$$\epsilon_2 = \frac{8}{2\pi\omega^2} \sum\nolimits_{mm} \int \frac{|P_{mm}(k)|^2 \, ds_j}{\nabla\omega_{mm}(k)} \tag{26}$$

$$n(\omega) = n(\omega) + ik(\omega) \tag{27}$$

$$R(\omega) = \frac{(n(\omega) - 1)^2 + k(\omega)^2}{(n(\omega) + 1)^2 + k(\omega)^2} \tag{28}$$

$$\sigma\omega = 2\omega_{ev}\frac{\hbar}{E_0} \tag{29}$$

$$\alpha(\omega) = \sqrt{2\omega}\sqrt{\{\varepsilon_1\omega^2 + \varepsilon_2\omega^2\}^{1/2} - \varepsilon_1(\omega)} \tag{30}$$

The real part and complex part of the frequency-dependent DF are indicated by $\varepsilon_1(\omega)$ and $\varepsilon_2(\omega)$. In Table 3, all computed data of optical parameters are mentioned for pure and doped material. At 0 eV, the static values of IDF ($\varepsilon_1(0)$) manifest the decreasing mode for pure BTO in contrast increasing mode reveals for $Ba_{0.75}Ra_{0.25}TiO_3$, $Ba_{0.50}Ra_{0.50}TiO_3$ and $Ba_{0.25}Ra_{0.75}TiO_3$-doped materials divulged in Table 4.

From Table 4, the computed values of dielectric function are decreased continually but in case of (0.75Ra) enhanced very solely and absorption increased with increasing the doping concentration (x). But in case of refractive index the calculated values are decreased and reflectivity of $Ba_{0.75}Ra_{0.25}TiO_3$, $Ba_{0.50}Ra_{0.50}TiO_3$ and $Ba_{0.25}Ra_{0.75}TiO_3$-doped materials smallest as compared to pure (BTO). The refractive index determines how light propagates through a medium. A lower refractive index means that light will travel faster in that medium compared to surrounding materials. This can lead to effects such as reduced refraction, smaller angles of incidence, and potentially changes in the overall path of light rays. Decreasing the refractive index can impact the functionality of optical devices. For example, in lenses, a lower refractive index can result in weaker focusing power, reducing the ability to converge or diverge light. In waveguides or optical fibers, a decreased refractive index can alter the guiding properties and affect the transmission of light through these structures. The dielectric function is related to the reflectivity of a material. A decrease in the dielectric function can lead to reduced reflection of light at the interface between two media. This property is often desired in applications like anti-reflective coatings or optical coatings to minimize unwanted reflections and enhance light transmission. The dielectric function is also related to the absorption of electromagnetic energy. A decrease in the dielectric function can imply a reduction in energy absorption in a material,

Table 4
Computed data of optical responses of pure (BTO) and $Ba_{0.75}Ra_{0.25}TiO_3$, $Ba_{0.50}Ra_{0.50}TiO_3$ and $Ba_{0.25}Ra_{0.75}TiO_3$ materials.

Materials	$\boldsymbol{\varepsilon_1}$	α(ω)	$\boldsymbol{R(\omega)}$	$\boldsymbol{n(\omega)}$
Theoretical/Other Work	4.67 Adil AlShoaibi et al.	0.002	0.56	2.96
Pure (BTO)	8.83	0	0.25	2.97
$Ba_{0.75}Ra_{0.25}TiO_3$	8.67	0.003	0.24	2.90
$Ba_{0.50}Ra_{0.50}TiO_3$	8.43	0.052	0.20	2.89
$Ba_{0.25}Ra_{0.75}TiO_3$	8.81	0.098	0.19	2.66

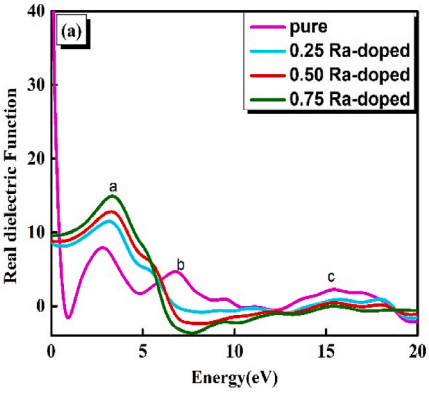

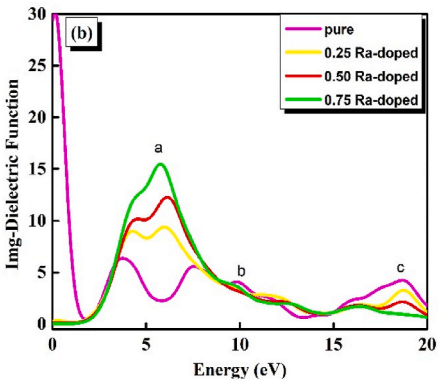

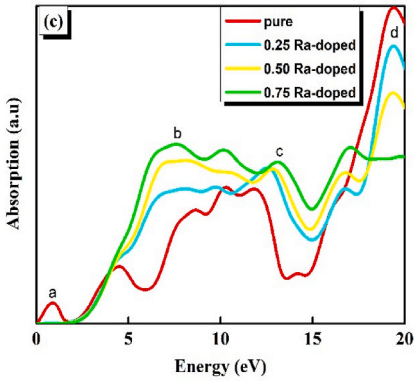

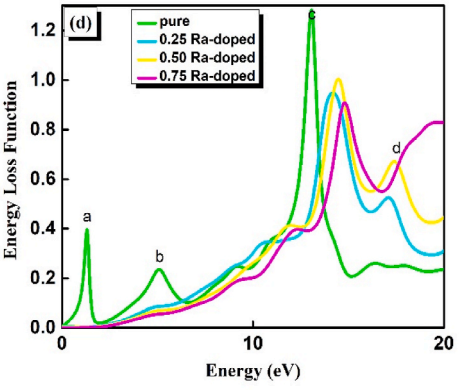

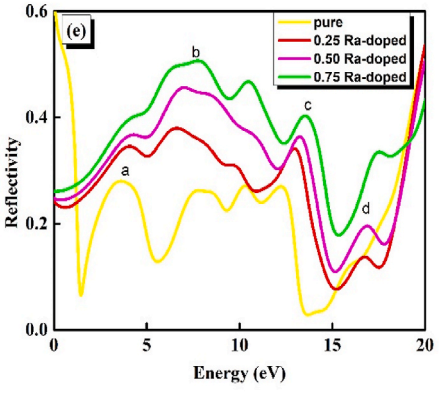

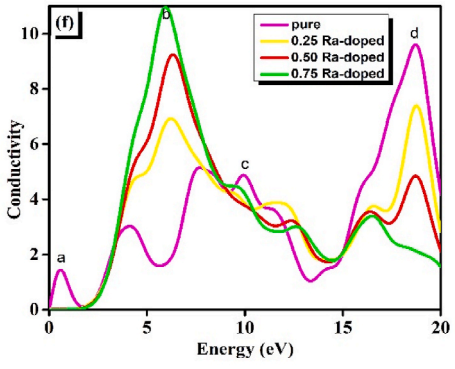

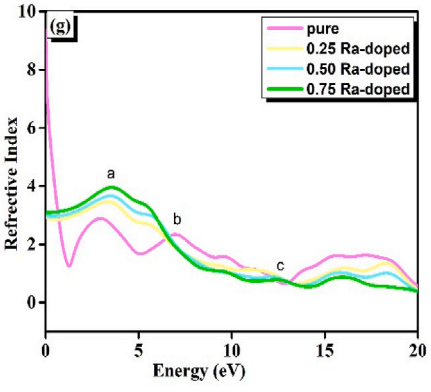

(caption on next page)

Fig. 7. Before and after doped inoculation: (a, b) real and imaginary parts of DF; (c) absorption; (d) energy loss function; (e) reflectivity; (f) conductivity and (e) real part of refractive index.

leading to lower energy dissipation or heat generation when exposed to electromagnetic fields or radiation. Refractive index and dielectric function are influenced by the electronic structure and polarization response of a material. Changes in these values can indicate alterations in the material's composition, density, or molecular structure. Thus, a decreased refractive index or dielectric function may indicate modifications in the optical and electrical properties of a material. It's important to note that the specific consequences of decreased refractive index and dielectric function depend on the application, material, and the range of wavelengths under consideration. Different fields, such as optics, photonics, and materials science, may interpret and utilize these changes differently based on their specific requirements and objectives. The computed optical parameters of pure (BTO) and $Ba_{0.75}Ra_{0.25}TiO_3$, $Ba_{0.50}Ra_{0.50}TiO_3$ and $Ba_{0.25}Ra_{0.75}TiO_3$-doped materials as shown in Fig. 7.

Hence, for pure BTO, $\varepsilon_1(\omega)$ is pretended in Fig. 7(a). The main three peaks of pure BTO and doping concentration (x) materials are about 14.82 (0.75Ra), 4.66 (BTO) and 2.22 (BTO) at energy ranges are noted 3.32eV, 6.81eV and 15.34eV respectively. This ensues due to O-2p state electrons transit to the Ti-3d state at X-symmetry point in momentum space. While Img part of dielectric function is revealed in Fig. 7(b), for pure $BaTiO_3$ and $Ba_{0.75}Ra_{0.25}TiO_3$, $Ba_{0.50}Ra_{0.50}TiO_3$ and $Ba_{0.25}Ra_{0.75}TiO_3$-doped materials it has high intensity peaks are obtained 15.48 (0.75Ra), 4.11 (BTO) and 4.18 (BTO) at energy ranges are 5.75eV, 9.86eV and 18.67eV being of O-2p state electrons transit to the Ba-6p state at R-symmetry point. Therefore, these measured readings demonstrate the variation in peak values. Meanwhile, the values of maximum peaks of $\varepsilon_2(\omega)$ is illustrated in above fig with different concentration doping the major peak values consistently decreases but in case of $Ba_{0.75}Ra_{0.25}TiO_3$, $Ba_{0.50}Ra_{0.50}TiO_3$ with different concentration doping, it can be seen that these values slightly decrease and eventually increases when shifting towards high energy spectrum. The dielectric function is a complex quantity that describes the response of a material to an external electric field. In the case of BTO, a ferroelectric material, the dielectric function is particularly interesting due to its unique properties. In the case of BTO, the real part of the dielectric function indicates its ability to support polarization, which is the displacement of positive and negative charges within the material. BTO is a ferroelectric material, which means it can exhibit spontaneous polarization even in the absence of an external electric field. The real part of the dielectric function accounts for the contribution of this polarization to the overall dielectric response. In BaTiO3, the imaginary part of the dielectric function is related to the loss mechanisms within the material, such as energy dissipation due to defects, impurities, or domain wall motion. It quantifies the amount of energy that is absorbed or dissipated by the material when an electric field is applied. By studying these components, researchers can gain insights into the polarization behavior, electrical conductivity, and energy dissipation mechanisms of BTO. Understanding these properties is crucial for various applications, including electronic devices, capacitors, sensors, and memory devices, where BaTiO3's unique ferroelectric behavior can be harnessed [68]. Fig. 7 (c) the prominent three peaks for pure BTO and $Ba_{0.75}Ra_{0.25}TiO_3$, $Ba_{0.50}Ra_{0.50}TiO_3$ and $Ba_{0.25}Ra_{0.75}TiO_3$-doped materials of absorption at applied neutral strain were found are 0.86eV, 7.63eV and 13.15eV energy values respectively. Both peaks are used outside the visible light spectrum. As can be observed, both BTO and (Ra)-doped BTO have a fairly wide absorption zone, with the best absorption section being located in the UV range. In particular, as compared to BTO and $Ba_{0.75}Ra_{0.25}TiO_3$, $Ba_{0.50}Ra_{0.50}TiO_3$ and $Ba_{0.25}Ra_{0.75}TiO_3$-doped materials, the absorption edge of Ra-doped BTO is shifted to the higher energy side. The blue-shift of the (Ra)-doped BTO have good optical absorption capability than BTO in the region, which could make doped concentration of BaTiO3 a strong valuable potential candidate for UV optoelectronic devices. The relationship between the optical BG and the absorption parameter is followed by

$$\alpha(\omega)\ \mathrm{hv} = c\ \left(\mathrm{hv} - E_g\right)^{\frac{1}{2}}$$

where h is called the Planck's coefficient, c is called a constant for a direct transition, v denotes the frequency of radiation, and α represents the optical absorption coefficient [69]. Additionally, the optical Eg of the BTO and $Ba_{0.75}Ra_{0.25}TiO_3$, $Ba_{0.50}Ra_{0.50}TiO_3$ and $Ba_{0.25}Ra_{0.75}TiO_3$-doped materials are determined by the given expression

$$E_g = (1-x)E_{g-BTO} + xE_{Ra,TO} - bx(1-x)$$

Where b denotes the bowing factor and $E_{Ra,TO}$ and E_{g-BTO} are the BG of materials BTO and $Ba_{0.75}Ra_{0.25}TiO_3$, $Ba_{0.50}Ra_{0.50}TiO_3$ and $Ba_{0.25}Ra_{0.75}TiO_3$-doped materials respectively. The plot of loss function is depicted in Fig. 7(d). The computed values of peak of L(ω) is narrated in above graph. The major contribution of peaks is noted 0.39 (BTO), 0.23 (BTO) and 1.27 (0.50Ra) at energy ranges are 1.29eV, 5.08eV and 1746eV respectively. According to it, when $BaTiO_3$ is doped with $Ba_{0.75}Ra_{0.25}TiO_3$ and $Ba_{0.50}Ra_{0.50}TiO_3$-doped materials it slightly arises but after $Ba_{0.25}Ra_{0.75}TiO_3$ it drastically falls comparatively pure $BaTiO_3$. Consequently, it can be noticed that the IDF and loss function have the inverse relationship between them. Fig. 7 (e) computed the value of reflectivity of pure and doped materials the maximum contribution of main three peaks are noted 0.27 (BTO), 0.50 (0.75Ra) and 0.19 (0.50Ra) at energy ranges are obtained 3.75eV, 7.71eV and 16.87eV respectively. As it is the reflectivity and absorption have also inverse relation between them because the point where the value of reflectivity is higher exactly at that point the value of absorption becomes low. Similarly, the refractive index and absorption both are inversely proportion. These results confirm the semiconductor behavior of material. Fig. 7 (f), computed the conductivity of pure and dopant materials, the prominent contribution noted four important edges are 1.39 (BTO), 10.95 (0.75Ra) and 9.57 (BTO) at energy ranges are 0.58eV, 5.94eV and 9.94eV respectively. The conductivity is connected to the electron concentration and mobility. Changes in electron attention and mobility are what cause the change in conductivity. Non-degenerate semiconductors that have been frivolously doped have slightly different mobility that can be determined by parameters [70]. Therefore, the enhancement in electron involvement results in an enhancement in the conductivity of pure and $Ba_{0.75}Ra_{0.25}TiO_3$,

$Ba_{0.50}Ra_{0.50}TiO_3$ and $Ba_{0.25}Ra_{0.75}TiO_3$-doped materials. The significance of understanding the conductivity function of $BaTiO_3$ lies in its numerous applications in electronic devices. $BaTiO_3$ is widely used in the production of capacitors, sensors, actuators, and other components. By controlling the conductivity of $BaTiO_3$ through external electric fields or temperature changes, its electrical properties can be tailored to suit specific applications. For example, in capacitors, BTO high dielectric constant and tunable conductivity function allow for the storage and release of electrical charge. Fig. 7 (g), it is evident that the refractive index is a computed capacity that is confidentially associated with microscopic atomic interaction which delivers data about how much light is bent or refracted by a substance. The remarkable four main edges computed for pure of pure and $Ba_{0.75}Ra_{0.25}TiO_3$, $Ba_{0.50}Ra_{0.50}TiO_3$ and $Ba_{0.25}Ra_{0.75}TiO_3$-doped materials are 3.96 (0.75Ra), 2.32 (BTO) and 0.81 (0.75Ra) at 3.59eV, 6.92eV and 12.64eV respectively. All optical

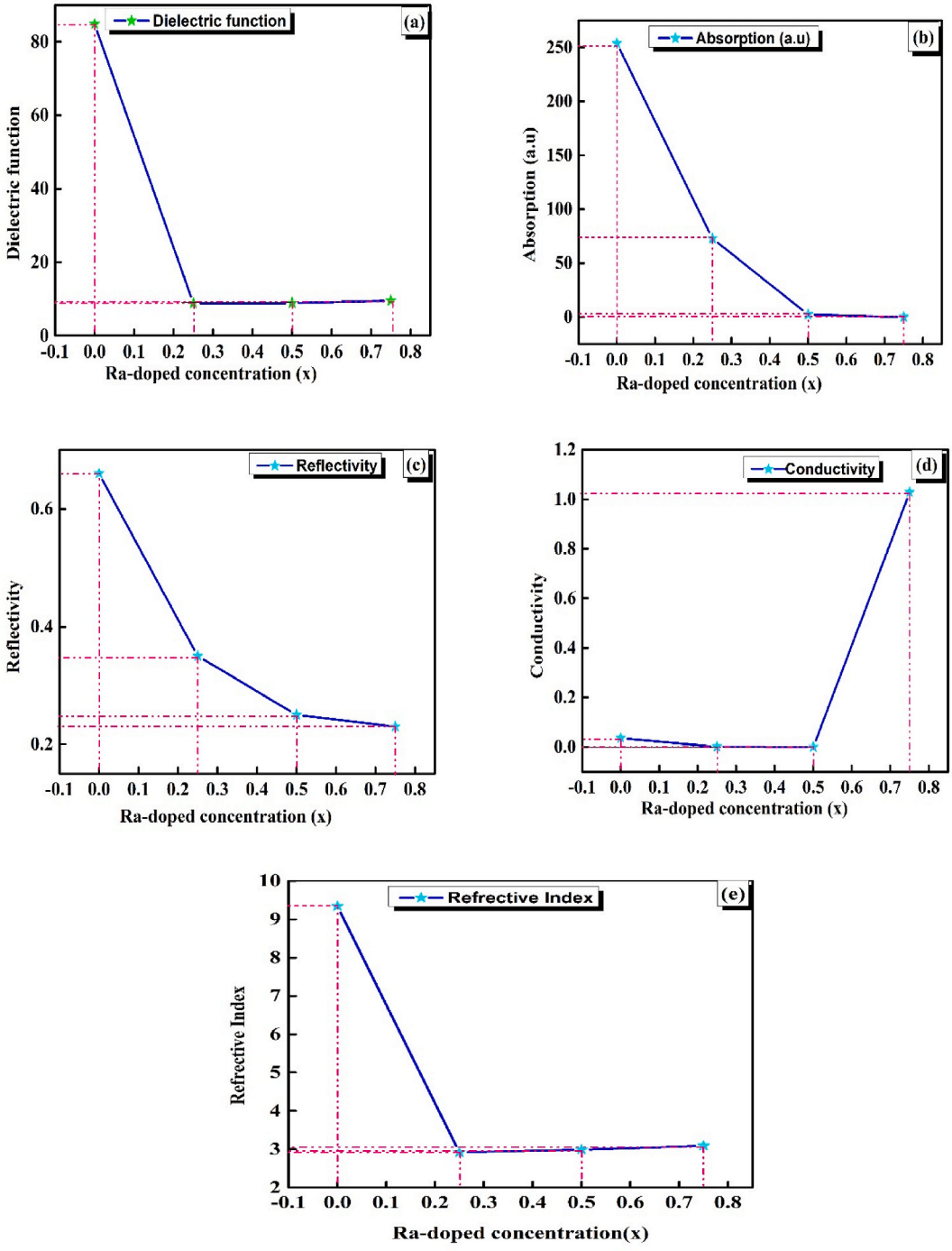

Fig. 8. Before and after doped inoculation trends: (a) Real DF; (c) Absorption; (d) reflectivity; (f) conductivity and (e) refractive index.

parameters are estimates the energies range from 0 eV up to 20eV. The calculated optical parameter trends before and after doping as shown in Fig. 8.

The computed trends of optical parameters with respect to enhanced doping concentration (x) as shown in Fig. 8.

From Fig. 8 (a to e) calculated the main trends of optical responses of pure and doped materials. With increasing doping concentration (x) the dielectric function and reflective index values are generated decreasing trends. While, the absorption and conductivity trends shown increased value continually with increasing doping concentration (x) respectively. The refractive index is a fundamental parameter that influences how light interacts with matter. Its significance lies in its ability to describe and predict the behavior of light in different materials, enabling advancements in optics, material science, telecommunications, and various other scientific and technological fields. These outcomes illustrated that the pure and doped $BaTiO_3$ is a potential candidate for ultraviolet devices [29]. Hence, the values of n(0) arises fall for $Ba_{0.75}Ra_{0.25}TiO_3$, $Ba_{0.50}Ra_{0.50}TiO_3$ materials doping in $BaTiO_3$ as compare to pure material which is reported in Table 4. This increase in n(ω) relates to the zero-absorption energy.

3. Conclusion

In summary, we have systematically investigated the structural, electronic, mechanical and optical performance of pure Barium titanate ($BaTiO_3$) and $Ba_{0.75}Ra_{0.25}TiO_3$, $Ba_{0.50}Ra_{0.50}TiO_3$ concentrations have been employed by first-principles computations. It is found that the different concentration (x) of Ra for A-site leads to more significant lattice distortion and prominent enhance in the bond lengths of Ra–O, Ba–O and Ti–O respectively. When the impurities (X = 0, 0.50, 0.75) of Ra^{+2} for the suitable Ba^{+2}site, the CB and VB to shift to a smaller energy state and its impact on band gap engineering shift from an indirect to a direct band gap at symmetric point (X-G). We found that the atomic states (Ti-3d), (Ba-6s), (Ba-3p), and (O-2p) all strongly contribute to the Fermi level. The extraordinary contribution of Ti atoms in the (3d) and (3p) states indicates that they play a more significant role close to the Fermi level Ef. By considering the elastic parameter and mechanical responses, the material was establishing to be mechanically stable and showed ductile and anisotropic nature. The Kleinman coefficient (ξ), it is clear that (Ra)-doped materials shows slightly large resistance to bond bending and bond angle distortion as compare to pure $BaTiO_3$. When enhanced the concentration of (Ra^{+2}) for the (Ba^{+2}) site decreased the value of dielectric coefficient and refractive index values as compare to pure $BaTiO_3$. Additionally, the different impurities of Ra-doped, decreases the reflectivity of the BTO, and transparence remain same before and after doping materials. The computed optical responses indicate that (Ra)-doped BTO lead to the good improvement of the UV-light photocatalytic ability. Whereas opacity is in the ultraviolet range of 10^{-13}eV and beyond 20 eV have large potential application in next generation opto-electronic devices.

Consent for publication

Not applicable.

Ethics approval and consent to participate

Not applicable.

Funding

Not applicable.

Availability of data and materials

Not applicable.

CRediT authorship contribution statement

Muhammad Moin: Writing – review & editing, Writing – original draft, Project administration. **Abdul Waheed Anwar:** Supervision. **Mehrunisa Babar:** Writing – review & editing, Formal analysis. **Udayabhaskararao Thumu:** Formal analysis. **Anwar Ali:** Investigation.

Declaration of competing interest

The authors declare that they have no known competing financial interests or personal relationships that could have appeared to influence the work reported in this paper.

References

[1] J. Sun, Y. Li, Research on improving energy storage density and efficiency of dielectric ceramic ferroelectric materials based on BaTiO3 doping with multiple elements, Journal of Composites Science 7 (6) (2023) 233.

[2] J. Liu, et al., Ferroelectric–optoelectronic hybrid system for photodetection, Small Methods (2023) 2300319.
[3] R. Sengwa, N. Kumar, M. Saraswat, Morphological, structural, optical, broadband frequency range dielectric and electrical properties of PVDF/PMMA/BaTiO3 nanocomposites for futuristic microelectronic and optoelectronic technologies, Mater. Today Commun. 35 (2023) 105625.
[4] J. Yan, et al., Tuning dielectric properties of sputtered BaTiO3 thin film capacitors via multilayering with SrTiO3, Functional Materials Letters 16 (2) (2023) 2340012.
[5] L. Zhen, et al., Flexible inorganic piezoelectric functional films and their applications, Journal of Advanced Ceramics 12 (3) (2023) 433–462.
[6] Y.B. Adediji, et al., *A review of energy storage applications of lead-free BaTiO3-based dielectric ceramic capacitors.* Energy, Ecol. Environ. (2023) 1–19.
[7] C. Li, et al., Rare earth-based nanomaterials in electrocatalysis, Coord. Chem. Rev. 489 (2023) 215204.
[8] S. Islam, et al., Effects of yttrium doping on structural, electrical and optical properties of barium titanate ceramics, Heliyon (9) (2022) 8.
[9] A. Alshoaibi, et al., Insights into the impact of yttrium doping at the Ba and Ti sites of BaTiO3 on the electronic structures and optical properties: a first-principles study, ACS Omega 5 (25) (2020) 15502–15509.
[10] Z. Hasan, et al., Influence of Ca doping in structural, electronic, optical and mechanical properties of Ba1− xCaxTiO3 perovskite from first-principles investigation, Sci. Rep. 13 (1) (2023) 10487.
[11] Sumona, H., et al., *Investigation Of Structural, Electrical And Optical Properties of Lanthanum and Zirconium Doped Barium Titanate Ceramics.* Electrical and Optical Properties of Lanthanum and Zirconium Doped Barium Titanate Ceramics..
[12] N. Ortega, et al., Multifunctional magnetoelectric materials for device applications, J. Phys. Condens. Matter 27 (50) (2015) 504002.
[13] P. Guan, et al., Effect of Sm3+ doping on ferroelectric, energy storage and photoluminescence properties of BaTiO3 ceramics, Ceram. Int. 49 (8) (2023) 11796–11802.
[14] S. Gillani, et al., Stimulated band structure by external isotropic static pressure and its impact on optoelectronic properties of PbZrO3: an ab-initio calculation, Optik 241 (2021) 167024.
[15] S.S. Köcher, Simulation of Static and Dynamic Magnetic Resonance Parameters for Solid Mixed Conductors, Dissertation, RWTH Aachen University, 2019, 2019.
[16] R. Roth, et al., Phase equilibria and crystal chemistry of the binary and ternary barium polytitanates and crystallography of the barium zinc polytitanates, J. Solid State Chem. 104 (1) (1993) 99–118.
[17] I. Derkaoui, et al., Overview of the structural, electronic and optical properties of the cubic and tetragonal phases of PbTiO3 by applying hubbard potential correction, Materials 16 (12) (2023) 4302.
[18] Q.D. Ho, D.K. Nguyen, H.A. Huy, Computational study of hyperfine interaction for Zn substitute Ga in β-Ga2O3, Computational Condensed Matter 32 (2022) e00727.
[19] A. Azcatl, et al., Near-unity photoluminescence quantum yield in MoS2, J. Phys. Chem 100 (117) (2013) 10229–10243.
[20] R. Terki, et al., Full potential calculation of structural, elastic and electronic properties of BaZrO3 and SrZrO3, Physica status solidi (b) 242 (5) (2005) 1054–1062.
[21] M. Siddiqui, et al., Phase transformation of cold-sintered doped barium titanate ceramics during the post-annealing process, Open Ceramics (2023) 100401.
[22] Z. Chen, et al., Optimizing energy storage properties under moderate electric fields in Na0. 5Bi0. 5TiO3-based ceramics via configuration entropy modulation, Ceram. Int. (2023).
[23] Z. Hu, et al., Enhanced piezoelectricity in Na and Ce co-doped CaBi 4 Ti 4 O 15 ceramics for high temperature applications, J. Adv. Ceram. (2023).
[24] A.A. Demkov, A.B. Posadas, Integration of functional oxides with semiconductors 25 (2014). Springer.
[25] A.J. Hatt, Influence of Strain on the Structural Instabilities and Functional Properties of Complex Oxides, University of California, Santa Barbara, 2010.
[26] S. Aoyagi, et al., Composite structure of BaTiO3 nanoparticle investigated by SR X-ray diffraction, J. Phys. Soc. Jpn. 71 (5) (2002) 1218–1221.
[27] D. Bilc, et al., Hybrid exchange-correlation functional for accurate prediction of the electronic and structural properties of ferroelectric oxides, Phys. Rev. B 77 (16) (2008) 165107.
[28] S. Wemple, M. Didomenico Jr., I. Camlibel, Dielectric and optical properties of melt-grown BaTiO3, J. Phys. Chem. Solid. 29 (10) (1968) 1797–1803.
[29] R.A. Evarestov, A.V. Bandura, First-principles calculations on the four phases of BaTiO3, J. Comput. Chem. 33 (11) (2012) 1123–1130.
[30] J. Junquera, et al., First-principles calculation of the band offset at B a O/B a T i O 3 and S r O/S r T i O 3 interfaces, Phys. Rev. B 67 (15) (2003) 155327.
[31] Z. Teng, et al., The electronic structures and optical properties of B, C or N doped BaTiO3, AIP Adv. (9) (2018) 8.
[32] M. Solayman, et al., A deep dive into structural, electronic, optical, and mechanical properties of ATiO3 (A= Ba, Th): DFT insights, Phys. Scripta 98 (12) (2023) 125944.
[33] S. Sanna, et al., Barium titanate ground-and excited-state properties from first-principles calculations, Phys. Rev. B 83 (5) (2011) 54112.
[34] E. Ching-Prado, Stress dependence of structure, electronic and optical properties of BaTiO3 from WC, VdW-DF-C09 and HSE functional calculations, Ferroelectrics 535 (1) (2018) 171–182.
[35] L. Wu, B. Luo, E. Tian, Ferroelectric properties of BaTiO3-BiScO3 weakly coupled relaxor energy-storage ceramics from first-principles calculations, J. Alloys Compd. 866 (2021) 158933.
[36] A.A. Adewale, et al., First principles calculations of structural, electronic, mechanical and thermoelectric properties of cubic ATiO3 (A= Be, Mg, Ca, Sr and Ba) perovskite oxide, Computational Condensed Matter 28 (2021) e00562.
[37] J. Mattina, et al., VIB1. Controlled oxygen vacancies and space correlation with Cr°t in SrTiO3, F, La. Properties Of Perovskites And Other Oxides 80 (2010) 347.
[38] P. Martins, et al., Advances in printing and electronics: from engagement to commitment, Adv. Funct. Mater. (2023) 2213744.
[39] Mirza, A.S., et al., *Sulphur-doped Copper (I) Iodide As Record Figure of Merit P-type Transparent Conductor.* Available at SSRN 4450373..
[40] P. Zhang, et al., Quantum size-dependent luminescence and nonlinear optical properties of silicon quantum dots/SiO2 multilayer, Opt Laser. Technol. 157 (2023) 108706.
[41] D.M. Nivedhitha, S. Jeyanthi, Polyvinylidene fluoride, an advanced futuristic smart polymer material: a comprehensive review, Polym. Adv. Technol. 34 (2) (2023) 474–505.
[42] Y.N. Hwang, et al., Evolution of the surface energy of BaTiO3 nanoparticles in the course of dispersant coating; an inverse gas chromatography study, Colloids Surf. A Physicochem. Eng. Asp. (2023) 131888.
[43] F. Wu, et al., Inorganic–organic hybrid dielectrics for energy conversion: Mechanism, strategy, and applications, Adv. Funct. Mater. (2023) 2212861.
[44] A. Fabbrizio, et al., Ra-partitioning between phlogopite and silicate melt and 226Ra/Ba–230Th/Ba isochrons, Lithos 114 (1–2) (2010) 121–131.
[45] L. Abdellahoum, Université Mohamed Boudiaf, M'silaCalculation of Structural, Electronic, Elastic and Optical Properties of 2H-CuGaO2: First Principle Study, 2017.
[46] S. Bhoobash, N. Pradhan, C. Behera, Tuning electrical properties of BaTiO3 with iron modification, Ceram. Int. (2023).
[47] Z.P. Feng, et al., Ultrasmall barium titanate nanoparticles modulated stretchable dielectric elastomer sensors with large deformability and high sensitivity, InfoMat (2023) e12413.
[48] B.J. Sahariah, et al., *A novel strategy to design lattice structures with zero Poisson's ratio.* Engineering Structures 288 (2023) 116214.
[49] S. Maity, et al., *Morphotropic Phase Boundary-Assisted Lead-Free BaTiO3/PDMS Composite-Based Hybrid Energy Harvester: A Portable Power Source for Wireless Power Transmission.* ACS Applied Energy Materials, 2023.
[50] Y. Huang, et al., Phase evolution and strong temperature-dependent electrostrictive effect in (1−x) Pb (Mg1/3Nb2/3) O3-xPbTiO3 solid solutions, J. Am. Ceram. Soc. 106 (8) (2023) 4709–4722.
[51] C. Long, et al., Simultaneously realizing ultrahigh energy storage density and efficiency in BaTiO3-based dielectric ceramics by creating highly dynamic polar nanoregions and intrinsic conduction, Acta Mater. (2023) 119135.
[52] Shah, V., et al., Exploring the Tunability of Lead Free Ba 0.5 Sn 0.5 Tio 3 to Mimic Pbtio 3. Available at SSRN 4420305..
[53] H. Mei, et al., Elastic Anisotropy and its Temperature Dependence for Cubic Crystals Revealed by Molecular Dynamics Simulations. Modelling and Simulation in Materials Science and Engineering, 2023.
[54] A. Sultana, et al., Enhanced optoelectronic activity of lead-free halide perovskites KMBr3 (M= Ge, Sn) under hydrostatic pressure, Phys. Scripta (2023).

[55] I. Gheewala, Multiscale Modelling of Nanoindentation of Multi-Layered Systems, Loughborough University, 2010.
[56] N. Pandech, K. Sarasamak, S. Limpijumnong, Elastic properties of perovskite ATiO3 (a= be, mg, Ca, Sr, and Ba) and PbBO3 (B= Ti, Zr, and Hf): first principles calculations, J. Appl. Phys. (17) (2015) 117.
[57] A.P. Sakhya, Electronic structure and elastic properties of ATiO3 (A= Ba, Sr, Ca) perovskites: a first principles study, Indian J. Pure Appl. Phys. 53 (2) (2015) 102–109.
[58] M. Liton, et al., Anisotropic elastic, opto-electronic and photocatalytic properties of BaTi2O5: first-principles calculations, Mater. Sci. Eng., B 296 (2023) 116658.
[59] A. Bezzalla, M. Elchikh, N. Iles, Multiferroic and half-metallic character of hexagonal BaTi0. 5Fe0. 5O3: DFT based calculation, Phil. Mag. (2023) 1–14.
[60] B. Hartmann, *12. Further Mechanical Techniques*, in *Methods in Experimental Physics*, Elsevier, 1980, pp. 59–135.
[61] J. Munir, et al., Physical properties of elastically and thermodynamically stable magnetic AcXO3 (X= Cr, Fe) perovskite oxides: a DFT investigation, Phys. Scripta 98 (6) (2023) 65513.
[62] S.C. Omowunmi, Modelling the Non-linear Dynamics of Polymer Solutions in Complex Flows, The University of Manchester, United Kingdom, 2011.
[63] A. Morandi, ETH ZurichNonlinear Light Generation in Disordered Assemblies of Nanoparticles, 2023.
[64] H. Yue, et al., First-principle study on correlate structural, electronic and optical properties of Ce-doped BaTiO3, Crystals 13 (2) (2023) 255.
[65] R. Islam, et al., Metallic boro-carbides of A 2 BC (A= Ti, Zr, Hf and W): a comprehensive theoretical study for thermo-mechanical and optoelectronic applications, RSC advances 12 (51) (2022) 32994–33007.
[66] I. Mochol, J.G. Kirk, Radiative damping and emission signatures of strong superluminal waves in pulsar winds, Astrophys. J. 776 (1) (2013) 40.
[67] J.K. Kana, et al., Thermally tunable optical constants of vanadium dioxide thin films measured by spectroscopic ellipsometry, Opt Commun. 284 (3) (2011) 807–812.
[68] P. Behera, et al., Emergent ferroelectric switching behavior from polar Vortex lattice, Adv. Mater. 35 (23) (2023) 2208367.
[69] K. Kumar, Thin Film Linear Array Bolometer Devices as Thermal Detectors, University of Cincinnati, 2023.
[70] G. Choudhary, et al., Ionic liquids: environmentally sustainable materials for energy conversion and storage applications, Environ. Sci. Pollut. Control Ser. (2023) 1–21.